Die approbierte Originalversion dieser Diplom-/Masterarbeit ist in der Hauptbibliothek der Technischen Universität Wien aufgestellt und zugänglich.
http://www.ub.tuwien.ac.at

The approved original version of this diploma or master thesis is available at the main library of the Vienna University of Technology.
http://www.ub.tuwien.ac.at/eng

TECHNISCHE UNIVERSITÄT WIEN
Vienna University of Technology

ILSB

DIPLOMARBEIT

Finite element simulation of uniaxial periodic structures

ausgeführt zum Zwecke der Erlangung des akademischen Grades eines Diplom-Ingenieurs unter der Leitung von

Assoc.Prof. Dipl.-Ing. Dr.techn. Heinz Pettermann

Dipl.-Ing. Martin Schwab, BSc

E317

Institut für Leichtbau und Struktur-Biomechanik

eingereicht an der Technischen Universität Wien

Fakultät für Maschinenwesen und Betriebswissenschaften

von

Andreas Blum

Matrikelnummer 1028340

Oberzellergasse 18/19

1030 Wien

Wien, im September 2015 Andreas Blum

Acknowledgements

I would like to thank my thesis advisors Professor Heinz Pettermann and Martin Schwab for their invaluable support. Especially the positive and creative way of problem solving was inspiring during the discussions that led to the methods and results presented in the following work. I would also like to thank the rest of the ILSB staff whose competence and dedication results in a high standard in teaching I very much appreciated and benefitted from during the last years.

On another note, I thank Professor Manfred Kaltenbacher for acting as second examiner.

Furthermore I would like to thank my family for their patience, the interest they showed in this work and the confidence they expressed. I especially thank Stefanie for her patience, understanding and caring throughout the last years. This support makes me look forward to future challenges.

Abstract

The present thesis deals with a modelling technique for the efficient finite element simulation of structures that exhibit a periodic arrangement of substructures along one axis. This uniaxial periodically recurring small scale substructure is modelled as a unit cell with periodic boundary conditions and thus provides a representative model for the large scale structure. On one hand, this model enables the determination of effective structural properties in the sense of a homogenisation approach. On the other hand, the unit cell model provides a highly resolved representation of the large scale structure, which allows the examination of small scale effects in the sense of a localisation approach.

The periodic boundary conditions are derived for the uniaxial case and extended regarding the use of shell elements and the application to unit cells with uneven boundary faces. Furthermore, an algorithm is developed in the framework of the finite element software package ABAQUS and its scripting interface. This algorithm is able to automatically generate periodic boundary conditions for a wide range of unit cells.

The verification of the theoretical assumptions as well as their programmed implementation is conducted with the help of three example models of increasing complexity which are assessed with multiple reference solutions. The simulation results of the example models show that the presented unit cell approach is correctly representing the structure and thus suited for the determination of the effective structural properties as well as for the examination of small scale effects.

Keywords: finite element method, uniaxial periodicity, homogenisation, localisation, periodic boundary conditions, shell elements, uneven boundary faces, periodic unit cell.

Kurzfassung

Die vorliegende Arbeit befasst sich mit einem modellierungstechnischen Ansatz für die effiziente Finite Elemente Simulation von Strukturen, welche entlang einer Achse eine periodische Anordnung von Substrukturen aufweisen. Diese uniaxial periodisch wiederkehrende Substruktur kleiner Größenordnung liefert als Einheitszelle unter der Anwendung von periodischen Randbedingungen ein repräsentatives Modell der Struktur höherer Größenordnung. Im Sinne einer Homogenisierung dient dieses Modell zum einen zur Bestimmung der effektiven strukturellen Eigenschaften. Zum anderen stellt die Einheitszelle im Sinne einer Lokalisierung eine hochaufgelöste Repräsentation der Struktur höherer Größenordnung dar, an der Effekte kleiner Größenordnung untersucht werden können.

Die periodischen Randbedingungen werden für den uniaxialen Fall hergeleitet und hinsichtlich der Verwendung von Schalenelementen und der Anwendung auf Einheitszellen mit unebenen Randflächen erweitert. Des Weiteren wird im Rahmen des Finite Elemente Softwarepakets ABAQUS und dessen Programmierschnittstelle ein Algorithmus entwickelt, der eine automatische Erzeugung der periodischen Randbedingungen für eine Vielzahl von Einheitszellen realisieren kann.

Die Beurteilung der Gültigkeit der theoretischen Annahmen und deren programmierte Umsetzung erfolgt anhand dreier Beispielmodelle ansteigender Komplexität unter Heranziehung verschiedener Referenzlösungen. Die Simulationsergebnisse der Beispielmodelle zeigen, dass der präsentierte Einheitszellenansatz die Struktur korrekt repräsentiert und damit, sowohl die effektiven Eigenschaften ableiten als auch eine hochaufgelösten Darstellung von lokalen Effekten liefern kann.

Schlagwörter: Finite Elemente Methode, Uniaxiale Periodizität, Homogenisierung, Lokalisierung, Periodische Randbedingungen, Schalenelemente, Unebene Randflächen, Periodische Einheitszelle.

Contents

1. Introduction **1**

1.1. Background 1

1.1.1. Overview 1

1.1.2. Literature review 4

1.2. The present work 6

1.2.1. Motivation 6

1.2.2. Objectives 7

1.2.3. Scope 7

2. Theory **9**

2.1. Uniaxial periodic boundary conditions 9

2.2. Variables in Postprocessing 18

2.3. Nonlinear Effects 20

2.4. Torsion 21

3. Implementation **23**

3.1. Programming of the PBC Generator 23

3.1.1. General remarks 23

3.1.2. Model requirements and input 26

3.1.3. Algorithm to determine boundary nodes 27

3.1.4. Creating Periodic Boundary Conditions 28

3.1.5. Automated Postprocessing 29

3.1.6. Performance of the algorithm 29
3.2. Examples for verification 31
3.2.1. Example 1: Prismatic box beam 31
3.2.2. Example 2: Open circular cross section 34
3.2.3. Example 3: Perforated tube 38

4. Results and discussion **41**
4.1. Example 1: Prismatic box beam 41
4.1.1. Displacement 41
4.1.2. Stiffness 43
4.1.3. Stress 44
4.2. Example 2: Open circular cross section 47
4.2.1. Displacement 47
4.2.2. Stiffness 49
4.2.3. Stress 50
4.3. Example 3: Perforated tube 53
4.3.1. Displacement 53
4.3.2. Stiffness 54
4.3.3. Stress 55
4.3.4. Plasticity 61
4.4. Further Applications 64

5. Summary **66**
5.1. Outlook 68

A. Manual - Uniaxial PBC Generator **69**

Bibliography **77**

List of Figures

1.1. Exemplary definition of a plane periodic RUC (Image taken from [15]). 3
1.2. Practical examples for uniaxial periodic structures 4

2.1. Definition of the uniaxial periodic unit cell with control points 0^+ and 0^- and boundary faces f^+ and f^- 10
2.2. Basic concept of homogenisation at the example of uniaxial tension. Image based on [17]. 11
2.3. Possible uniaxial periodic load cases: tension, bending about two directions and torsion 12
2.4. Exemplary depiction of the contribution of a curvature to the displacement in p-direction due to bending about the u-axis. 15
2.5. a) Additional Control Points for a model based on continuum elements b) Exemplary depiction of a rotation about the u-axis 16
2.6. Two scenarios for boundaries that differ from the control points in p-direction 17
2.7. Exemplary for bending about the u-axis: The contribution to the cross sectional displacement due to a difference in p-direction of the undeformed boundaries. 18

3.1. Structure of algorithm that assigns PBC to an arbitrary uniaxial RUC model. 25

3.2. Total run time of the algorithm versus number of nodes 30
3.3. Cross section of the prismatic box beam in accordance with Dizy et al. [8]. 31
3.4. Four configurations of the prismatic box beam depicting the mesh and the PBC 33
3.5. Cross section of the thin walled open tube. 34
3.6. The two shell model configurations of the thin walled open tube depicting the mesh. 35
3.7. Anti-metric shear stress distribution due to torsion of a plane plate as representation for an open thin walled cross section. 36
3.8. Depiction of s-coordinate and distance definition according to [20]. . 37
3.9. Perforated tube: a) Flattened depiction of semicircle showing pattern and unit cell definition b) Cross section the of tube 39
3.10. FE models of perforated tube : a) Long tube with coupling boundary conditions b) RUC with PBC 39

4.1. Component-wise nodal displacements along the boundaries f^+ and f^- due to bending about the u-axis. 42
4.2. Contour plot of maximum principle stress of the different configurations for bending about the u-axis 45
4.3. Maximum principle stress over a segment of the path for all configurations. 46
4.4. Component-wise displacement due to torsional load along the corresponding boundaries f^+ and f^- as well as along a respective path of the long tube model. 48
4.5. Contour plot of torsional shear stress $|\tau_{\theta z}^{max}|$ of the RUC with 20-fold magnified depiction of the deformation. 51

4.6. Plot of the maximum shear stress over the circumference of the cut circle cross section 53
4.7. Component-wise nodal displacements due to torsional load in cylindrical r-θ-z system at the corresponding boundaries f^+ and f^-. . . 54
4.8. Contour plot of the in-plane shear stress $\sigma_{\theta z}$ due to torsional load: a) RUC model b) segment of the long tube model. 56
4.9. Shear stress $\sigma_{\theta z}$ due to torsion for a) twofold depiction of the RUC b) a depicted segment of the long tube model. 57
4.10. Stress component σ_{zz} (σ_{pp}) along circumferential paths of the RUC with a coarse mesh and the long tube model, see Fig. 4.8 for the definition of the hole paths. 58
4.11. Consideration of local shear stress field continuity at corresponding boundaries for a) a coarse mesh RUC arrangement and b) a fine mesh RUC arrangement. The view detail is defined corresponding to the dashed box in Fig. 4.9. 59
4.12. Stress components $\sigma_{\theta\theta}$, σ_{zz}, $\sigma_{\theta z}$ along the first half of the paths defined in Fig. 4.8 for the RUC model with refined mesh. 59
4.13. Von Mises equivalent stress along the hole edges of different types of hole intersections in the RUC with refined mesh and one hole of the long tube model. See Fig. 4.8 for the definition of the hole paths. 60
4.14. Plots for the tensile displacement controlled loading with a elastic ideal plastic material behaviour for the RUC and the long tube model. 62
4.15. Contour plot of von Mises equivalent stress due to maximum tensile loading with a linear-elastic ideal plastic material behaviour. 63
4.16. Comparison of von Mises equivalent stress on corresponding boundaries due to tensile loading and elastic ideal plastic material. 64

A.1. Input of data via RSG dialog for PBC generation 69

1. Introduction

1.1. Background

1.1.1. Overview

Computer aided engineering has become increasingly important in the modern product development process. Nearly every aspect of the product life cycle from the manufacturing process to the actual service conditions can be described by a numerical model. A simulation with the help of these models enables the engineer to gain important beforehand knowledge of a part's behaviour and how to improve its response most efficiently. The Finite Element Method (FEM) is one of the most powerful numerical methods to gain an approximate solution to several complex physical problems from thermal, electromagnetic, fluid and structural applications. The present work is dealing with the structural application, meaning the prediction and optimisation of a structure's mechanical response under load. Especially in lightweight design, where components are designed at the limit of their structural integrity, a reliable method that allows for time efficient modelling is key for a cost efficient product development process.

The FEM is based on the discretisation of a continuum with the respective element size determining the level of geometrical detail and the resolution of fields. The higher the level of detail is in a model, the better the actual structure is usually represented by the model. A high level of detail implies a high number of unknowns which has a direct influence on the computational demands. Despite the

drastic increase in computational power over the last decades, the use of modelling techniques that reduce the number of unknowns and thus the calculation time has remained very important.

Homogenisation and Localisation

Many complex structures consist of different levels of smaller substructures which in some cases have to be modelled in detail to obtain a reliable solution of the overall response. The levels of smaller substructures are best described by introducing the term of different length scales, meaning e.g. for a composite wing that small scale effects may relate to the ply level whereas large scale effects are associated to the global behaviour of the wing. Deducing effective properties from a small scale where the effect of local heterogeneities becomes apparent is known under the term of *homogenisation*. These effective properties regarding e.g. the structural stiffness can be applied to a large scale model in the next step and thus reduce modelling and computation time significantly. The term *localisation*, on the other hand, describes a method where the global response is adequately applied to the small scale yielding a highly resolved representation of the small scale effects due to inhomogeneities. Several methods have been developed to link the substructural behaviour to the global structure without losing the context of the global structure. These mathematical methods are termed multiscale methods and share the concept of linking different length scales which can be applied to a wide set of problems far beyond the presented use in computational mechanics.

Periodicity

One of these methods makes use of an internal periodicity of a structure in the sense that the structure is composed of a periodically recurring substructure, see Fig. 1.1. This recurring small scale structure is modelled as a Repeating Unit Cell

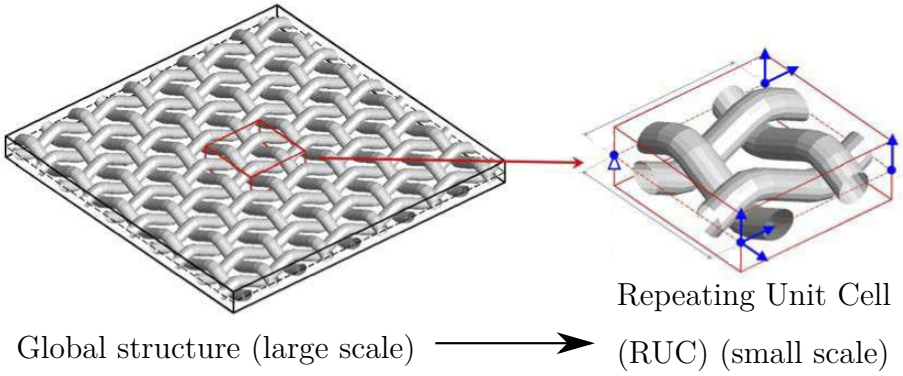

Figure 1.1.: Exemplary definition of a plane periodic RUC (Image taken from [15]).

(RUC) serving as a representation for the global structure. The boundaries of this unit cell are subjected to Periodic Boundary Conditions (PBC), so that the RUC provides a correct representation. Regarding the concept of homogenisation, the structural behaviour of this RUC with PBC serves as the basis to obtain the homogenised mechanical properties of the large scale structure.

Adapting the terminology used by Pahr [17], a general periodic structure can be categorised based on the number of axes of periodicity :

- one direction: uniaxial periodic
- two directions: plane periodic
- three directions: spatially periodic

The present work is confined to the consideration of *uniaxial periodic* structures. Examples of practical relevance for uniaxial periodicity in lightweight design are e.g. beam-like structures with a periodic arrangement along their main axis such as rotor blades, carbon nano tubes ([14]) or an aircraft fuselage. Figure 1.2 shows two examples with complex cross sections. Simulating e.g. the whole length of the rotor blade with the necessary level of detail will result in a time-consuming

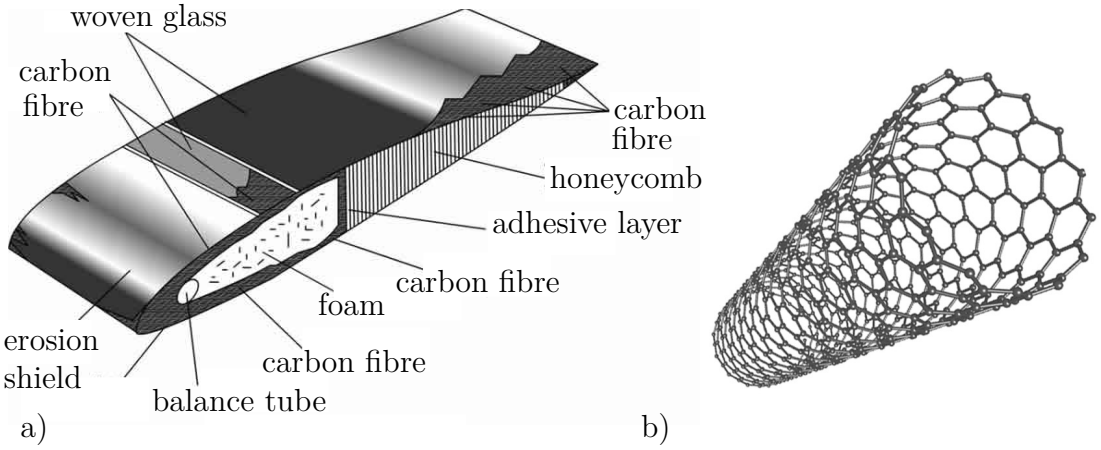

Figure 1.2.: a) Cross section of a composite rotor blade (Image based on [1]). b) Carbon nano tube (image taken from [2]).

modelling and high computational demands. By taking the periodicity along the main axis into account, the simulation of a single RUC representing one period is sufficient for the determination of the effective properties of the whole structure.

1.1.2. Literature review

An overview of where to find further information on the previously presented concepts as well as a short review of research related to the present work is given in the following section.

Most literature on the topic is found in relation to composite materials as these materials offer several length scales of heterogenous composition. Applications from the micromechanical consideration of the composites constituents or the determination of the effective behaviour of textile composites up to the homogenised properties of a complex laminated structure show the advantage of multiscale homogenisation techniques for this class of materials.

Referring to modelling strategies in micromechanics, Böhm [3] presents an overview of the concept of using periodic arrangements to obtain homogenised properties. Namely, a review of the current periodic microfield approaches and possible

unit cell definitions is given as well as an explanation of the basic concept of PBC by means of some examples. Pahr and Rammerstorfer [18] introduced plane periodic boundary conditions implicating a plane stress assumption and the use of volume elements. Gager et al. [10] as well as Hohe et al.[12] extended this approach for models based on shell elements.

Dizy et al. [8] used uniaxial periodic boundary conditions to obtain the effective properties of slender beam-like structures using volume elements which is closely related to the present work. In the work of Dizy et al. [8] a review of different techniques to gain effective properties for beam-like structures is given, see e.g. the work of Kolpakov [13] or Cesnik and Hodges [6], who applied the variational minimisation of the deformation energy to gain effective beam properties. Parts of the research of Dizy et al. [8] are replicated for the verification of the technical methods develop during the present thesis. Cartraud et al. [5] offer an extensive mathematical derivation of uniaxial periodic boundary conditions based on the asymptotic expansion method. Cartaud et al. [5] verify their approach with the determination of the effective properties of a stranded cable. The approaches of Dizy et al. [8] and Cartraud et al. [5] were both limited to the use of volume elements and even boundary faces.

Regarding the application of periodic boundary conditions to a finite element mesh, most approaches require a conformal mesh on the corresponding faces. Wippler et al. [24] bypassed this requirement by using projected periodic boundary conditions. A node triangle relating to a single corresponding node is used to set up the necessary equations instead of the common node-to-node relationship. Nguyen et al. [16] imposed periodic boundary conditions by the polynomial interpolation of the displacement field at the boundaries of the unit cell in order to circumvent the requirement of mesh conformity. Nevertheless the present work is limited to conformal meshes and further research could aim at implementing one

of the presented approaches for non-conformal meshes.

As for the technical realisation of the presented approach Wu et al. [25] show how PBC are implemented in a commercial FEM-Package for the spatial periodic case.

1.2. The present work

1.2.1. Motivation

The homogenisation of complex uniaxial periodic structures can be of great value, see e.g. Fig. 1.2. Accordingly, the previous section shows that research has already been conducted on this topic. However, the technical implementation of the homogenisation is a sophisticated task and not part of a commercial FEM package. It involves the following steps: (1) The choice and modelling of the representative periodic unit cell, (2) the application of PBC to the unit cell and (3) the simulation and evaluation of results to gain effective properties or the general response in case of path dependent small scale effects. Especially the application of the PBC and the evaluation of the results present a very time consuming task when conducted manually. This leads to the need for an automation of step (2) and (3). Besides that, the presented research reveals some limitations regarding step (1), i.e. the choice and modelling of the unit cell. So far, to the knowledge of the author, the use of shell elements for the modelling of uniaxial periodic unit cells has not been reported in the open literature. The use of shell elements is of particular interest for the modelling of stacked ply arrangements because they offer a considerable advantage in computational effort compared to a continuum element model (see e.g. the work of Davila et al. [7]). Furthermore only trivial boundary faces of the unit cell that are plane and perpendicular to the axis of periodicity are mainly considered in related research.

1.2.2. Objectives

The abovementioned limitations result in two main objectives for the present work.

The first objective is to extend the theory of uniaxial PBC regarding nontrivial boundaries and the use of shell elements.

Secondly, an automated generator of periodic boundary conditions is to be created that is able to process a wide range of geometrically possible uniaxial periodic unit cells. This automated generator is to work in the environment of a commercial FEM-Package.

In the present work the FEM-package ABAQUS/Standard 6.14-3 (*Dassault Systèmes Simulia Corp., Providence, RI, USA*) is utilised for all FEM-computations. The automation of different tasks is achieved with the Abaqus Scripting Interface which is an extension of the object-oriented programming language python (version 2.7.3, *Python Software Foundation, Delaware, USA*).

1.2.3. Scope

Based on the abovementioned objectives, this section aims to give a chapter wise outline of what is done to accomplish the defined goals.

The following chapter 2.1. *Theory* first gives a more detailed introduction to PBC followed by the derivation of the uniaxial PBC and their extension to a more general application with shell elements and nontrivial boundaries. Thereafter, the theoretical framework for the evaluation of the results is given by laying out the concept of how the effective properties are determined. Subsequently, a short consideration of the applicability of nonlinear effects to the presented method is provided. In addition to that, a short digression regarding the limitations of the torsional load case is given.

The chapter 3. *Implementation* is divided into the sections *Programming* and *Verification*. The section *Programming* presents how the theoretical groundwork is

put into practice with an automated generator of PBC. Selected methods and parts of the Python algorithm are presented in more detail and important information for the user of the generator are given regarding admissible and recommended input. Next, in the section 3.2. *Verification*, the example models are introduced which serve as verification for the developed method. The validity of the presented approach is assessed with analytical solutions, solutions of the literature as well as with related FEM-analyses.

In chapter 4. *Results and discussion* the results of the different verification simulations will be presented and discussed in detail.

The last chapter, 5. *Summary*, provides a short summary of the presented work leading to a conclusion of what has been achieved and an outlook on further relevant research.

The appendix consists of a manual for the automated generator including a step by step guide for the general user.

2. Theory

2.1. Uniaxial periodic boundary conditions

Basic requirements

In the following, periodic boundary conditions (PBC) for the uniaxial periodic case are derived. In the case of uniaxial periodicity, a segment of a large scale beam-like structure represents a periodically repeating unit cell (RUC) which is subjected to uniaxial PBC in order to provide a correct basis for the determination of the effective properties. Fig. 2.1 schematically shows how a RUC is taken out of the context of the larger uniaxial periodic structure. The resulting pair of free surfaces f^+ and f^- has to be coupled by the PBC. The superscripts $'-'$ and $'+'$ indicate which face the respective variable or term is attributed to. For the unit cell a orthonormal basis u, v, p is introduced with p representing the direction parallel to the direction of periodicity.

According to Böhm [3] the boundary conditions have to accomplish a behaviour of the faces f^+ and f^- so that the following requirements are met:

- *Geometric compatibility*: For both undeformed and deformed state the pairwise boundaries coupled by PBC have to be geometrically compatible. This means that no gaps, overlaps or unphysical constraints are allowed to occur with their fictitiously neighbouring unit cells.

- *Continuity*: A continuous field of all field variables must be given between corresponding boundaries. This implicates that the stress and strain field is

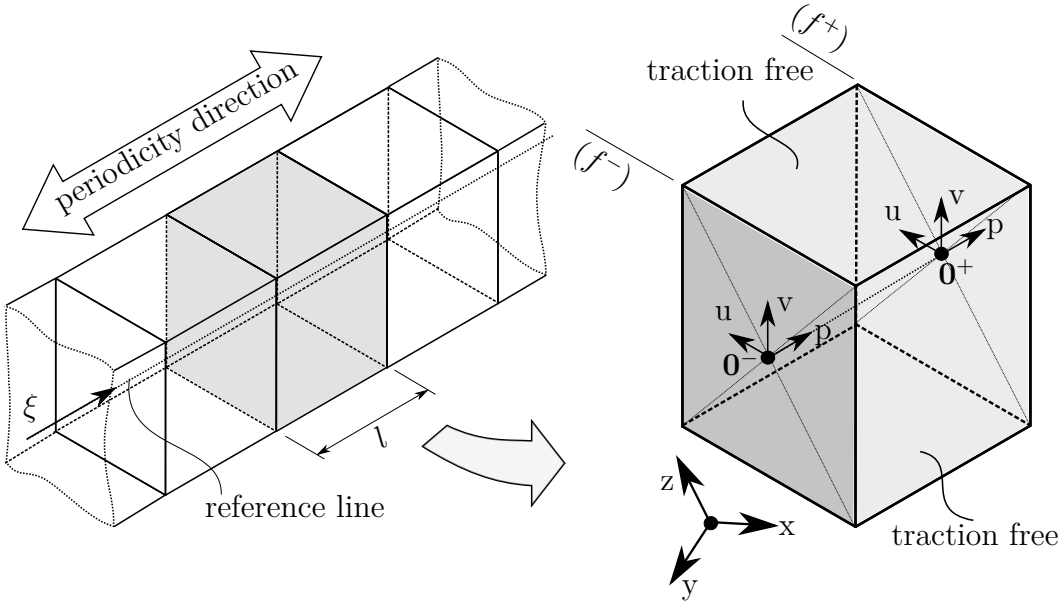

Figure 2.1.: Definition of the uniaxial periodic unit cell with control points 0^+ and 0^- and boundary faces f^+ and f^-

continuous on boundaries associated to each other. This requirement does not hold true for a discontinuity in the constitutive law relating strain and stress field as e.g. for boundaries that exhibit a material jump.

Furthermore the deformation energy has to be preserved over the scales, meaning that the deformation energy of the unit cell per unit length equals the one of the large scale structure.

The requirement of geometrical compatibility implies that coupled faces are equal up to a rigid body displacement (Pahr [17]). Enforcing this equality plus a rigid body displacement during the deformed configuration is essentially the job of the PBC.

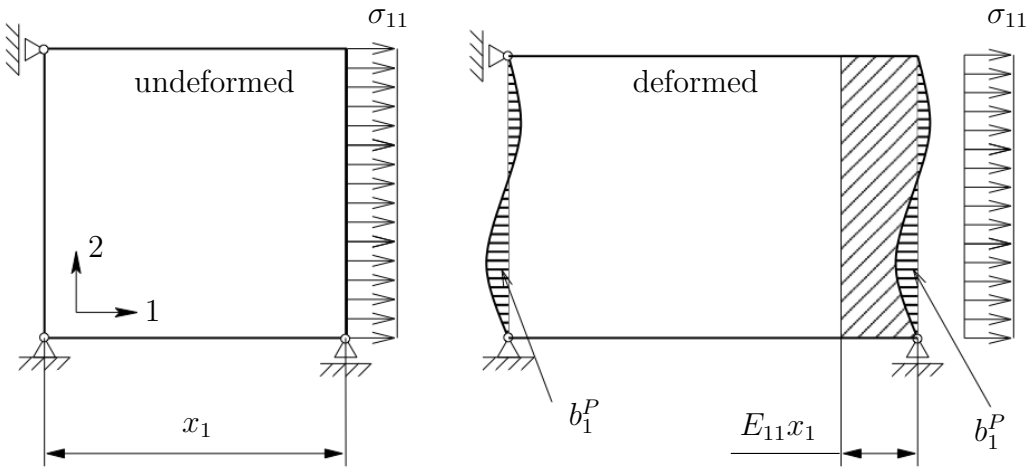

Figure 2.2.: Basic concept of homogenisation at the example of uniaxial tension. Image based on [17].

Derivation of the PBC

Pahr [17] stated for the spatial periodic case that a displacement field $b_i(\bar{x})$ at a position defined by the position vector $\bar{x}$ can be split into a constant displacement and a periodic displacement $b_i^P(x_i)$, see Fig. 2.2. The constant displacement is governed by the overall strain tensor $\mathbf{E}$ leading in index notation to,

$$b_i(\bar{x}) = E_{ij}x_j + b_i^P(\bar{x}) \quad . \tag{2.1}$$

For plane periodicity and uniaxial periodicity the relationship between $b_i^P(\bar{x})$and $b_i(\bar{x})$ is also influenced by the curvature χ_i of unit cell. Thus it is important to examine the valid load cases for uniaxial periodicity.

Following Gager [9] and a more detailed derivation from Cartraud et al. [5] or Buannic and Cartraud [4], respectively, the present work is limited to the first-order theory due to reasons of simplification. In consequence, this requirement results in the four load cases depicted in Fig. 2.3, namely Tension and Saint Venant's Torsion (see section 2.4) about the axis of periodicity as well as bending about

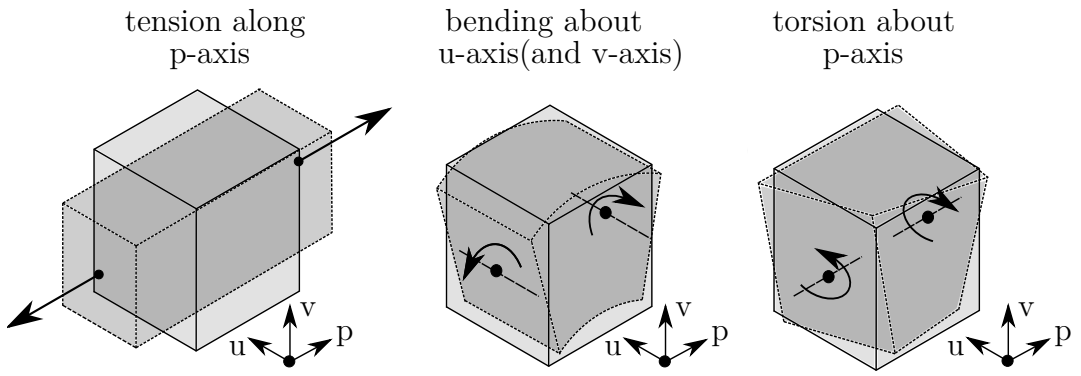

Figure 2.3.: Possible uniaxial periodic load cases: tension, bending about two directions and torsion

the u- and v-axis. These load cases represent the classical Euler-Bernoulli-Saint-Venant beam load cases, meaning that shear deformations in the cross section (cf. Timoshenko beam theory) are not discussed in the present work. In return this means that the present approach is especially well-suited for slender beam-like structures. Forging a bridge to the plane periodic case, the plane stress assumption of Pahr and Rammerstorfer [18] is transferred to the uniaxial periodic case, as it requires traction free faces on all directions but the one normal to the direction of periodicity. With the law of complementary shear stress it becomes apparent why a shear load other than an in-plane shear load e.g. due to torsion would result in the need for a traction exerted on faces other than the one normal to the direction of periodicity. In other words, a shear stress exerted on these faces would lead to a non periodic load scenario.

According to Dizy et al. [8] this leads for Eq. (2.1) to the following terms for

uniaxial periodicity,

$$b_u(\xi, u, v) = -\langle\chi_p\rangle v\xi + b_u^P(\xi, u, v) \quad , \tag{2.2}$$

$$b_v(\xi, u, v) = -\langle\chi_p\rangle u\xi + b_v^P(\xi, u, v) \quad , \tag{2.3}$$

$$b_p(\xi, u, v) = E_{\xi\xi}\xi - \langle\chi_v\rangle u\xi + \langle\chi_u\rangle v\xi + b_p^P(\xi, u, v) \quad . \tag{2.4}$$

Instead of a vector $\bar{x}$ in the case of spatial periodicity the uniaxial periodicity requires a single large scale coordinate ξ in the direction of periodicity (see Fig. 2.1) and the small scale coordinates u and v. For a unit cell with the length l the rigid body displacement between the boundaries is calculated in the deformed state as,

$$\Delta b_i(u, v) = b_i(\xi + l, u, v) - b_i(\xi, u, v) \quad . \tag{2.5}$$

Furthermore, it can be shown that (cf. [3], [17]),

$$E_{\xi\xi} = \langle\epsilon_{\xi\xi}\rangle = \frac{\Delta b_p}{l} \quad , \tag{2.6}$$

$$\langle\chi_i\rangle = \frac{\Delta\phi_i}{l} \quad , \tag{2.7}$$

hold for the averaged strain $\langle\epsilon_{\xi\xi}\rangle$ over the local unit cell, that can be expressed via the difference in translational displacement Δb_p of the corresponding faces divided by l. Accordingly, the mean curvatures $\langle\chi_i\rangle$ are expressed via the differences in rotational displacement $\Delta\phi_i$ of the corresponding faces divided by l. With the notation,

$$b_i(\xi + l, u, v) = b_i^+(u, v) \ , \ \ b_i(\xi, u, v) = b_i^-(u, v) \quad , \tag{2.8}$$

the general concept for periodic boundary conditions in the i-direction is described with,

$$b_i^+ = b_i^- + \Delta b_i \quad . \tag{2.9}$$

In other words, the displacement field on one boundary is a function of the displacement field of the corresponding boundary and the deformation state. In this

notation, Eqs. (2.2)-(2.4) with Eqs. (2.6)-(2.7) lead to the following uniaxial periodic boundary conditions,

$$b_u^+(u,v) = b_u^-(u,v) - \Delta\phi_p v + \Delta\phi_v p \quad , \tag{2.10}$$

$$b_v^+(u,v) = b_v^-(u,v) + \Delta\phi_p u - \Delta\phi_u p \quad , \tag{2.11}$$

$$b_p^+(u,v) = b_p^-(u,v) + \Delta b_p + \Delta\phi_u v - \Delta\phi_v u \quad , \tag{2.12}$$

$$\phi_u^+(u,v) = \phi_u^-(u,v) + \Delta\phi_u \quad , \tag{2.13}$$

$$\phi_v^+(u,v) = \phi_v^-(u,v) + \Delta\phi_v \quad , \tag{2.14}$$

$$\phi_p^+(u,v) = \phi_p^-(u,v) + \Delta\phi_p \quad . \tag{2.15}$$

The coordinates of the respective nodes on each face f^+ and f^- are u, v and p. Equations (2.13)-(2.15) refer solely to the application with shell elements providing a PBC coupling of the rotational degrees of freedom (DOF) of the respective shell elements at the corresponding boundaries. The terms $\Delta\phi_v p$ and $\Delta\phi_u p$ refer to nontrivial boundaries and are explained below. With respect to the load cases the terms in Eqs. (2.10)-(2.15) can be attributed as follows:

- Δb_p : tensile loading in p
- $\Delta\phi_u$: bending about u
- $\Delta\phi_v$: bending about v
- $\Delta\phi_p$: torsion about p

Figure 2.4 shows exemplary for a bending about the u-axis how the curvature or the rotation of the boundaries, respectively, contribute to the difference in displacement between corresponding nodes on f^- and f^+. To achieve the desired deformation state according to the four load cases or any superposition of them, a displacement controlled approach is chosen. The differences between the faces f^+ and f^- in displacement Δb_i and rotation $\Delta\phi_i$ are introduced via the control points

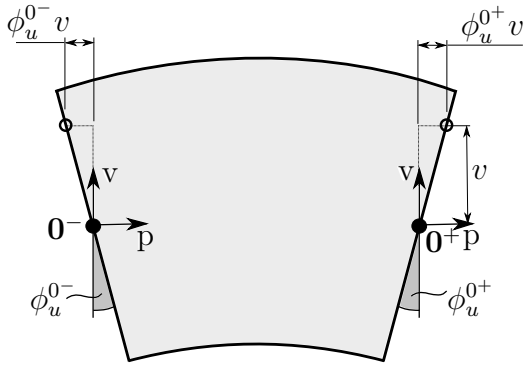

Figure 2.4.: Exemplary depiction of the contribution of a curvature to the displacement in p-direction due to bending about the u-axis.

(CP) 0^+ and 0^- (see Fig. 2.1). The choice of location of these CPs in relation to each other and to the unit cell underlies certain requirements and cannot be made arbitrarily. For a more detailed consideration of the choice of control points and its consequences for the unit cell behaviour see chapter 3 and appendix A. Other known names for these points in related research are *macroscopic degrees of freedom* or *master nodes*. In the case of a RUC based on shell elements the difference in rotational displacement is taken from the difference of the corresponding DOFs of the CPs,

$$\Delta\phi_u = \phi_u^{0+} - \phi_u^{0-} \quad , \tag{2.16}$$

$$\Delta\phi_v = \phi_v^{0+} - \phi_v^{0-} \quad , \tag{2.17}$$

$$\Delta\phi_p = \phi_p^{0+} - \phi_p^{0-} \quad , \tag{2.18}$$

$$\Delta b_p = b_p^{0+} - b_p^{0-} \quad . \tag{2.19}$$

Regarding the applicability of the boundary conditions from Eqs. (2.10)-(2.15) it is important to note that the equations are based on the small-angle approximation for trigonometric functions. An angle difference of $\Delta\phi_i < 6°$ is recommended for the error not to exceed 1%. This equals a rotation of the cell faces of $|\phi_i| < 3°$.

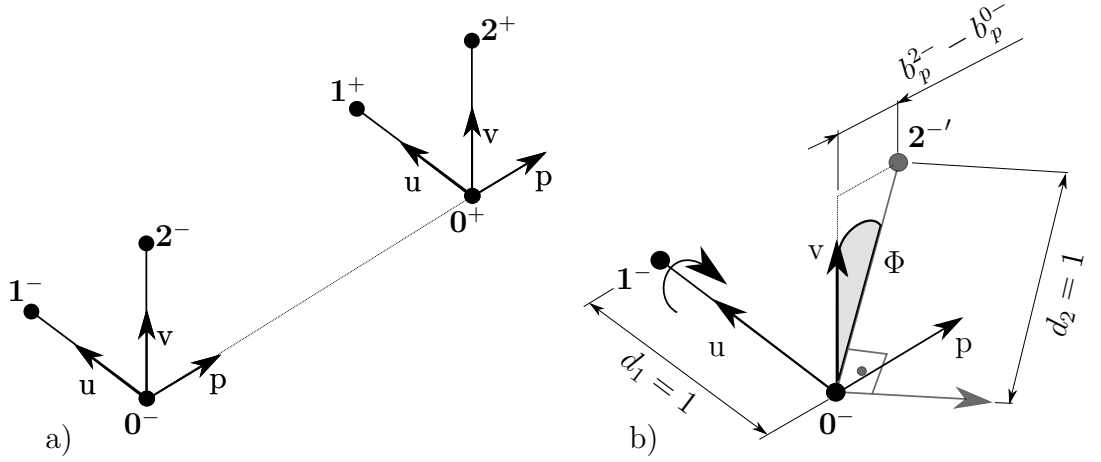

Figure 2.5.: a) Additional Control Points for a model based on continuum elements
b) Exemplary depiction of a rotation about the u-axis

Application to Volume Elements

When applying PBC to a model based on continuum elements the rotational DOFs of the CPs are not available. Hence, an alternative approach with two additional control points per face $1^{+/-}$ and $2^{+/-}$ is necessary to represent a rotation via a translational displacement (see e.g. Gager et al. [10]). Fig. 2.5 shows that the additional CPs are placed alongside the axes u and v with a distance of $d_1 = d_2 = 1$ for a simplified implementation later on. The calculation of the angle differences that are involved in Eqs. (2.10) to (2.15) is adjusted as,

$$\Delta\phi_u = \frac{1}{d_2}((b_p^{2+} - b_p^{0+}) - (b_p^{2-} - b_p^{0-})) \quad , \tag{2.20}$$

$$\Delta\phi_v = \frac{1}{d_1}((b_p^{0+} - b_p^{1+}) - (b_p^{0-} - b_p^{1-})) \quad , \tag{2.21}$$

$$\Delta\phi_p = \frac{1}{d_1}((b_v^{1+} - b_v^{0+}) - (b_v^{1-} - b_v^{0-})) \quad , \tag{2.22}$$

$$\Delta b_p = b_p^{0+} - b_p^{0-} \quad , \tag{2.23}$$

merely using the translational DOFs of the control points to express a rotation.

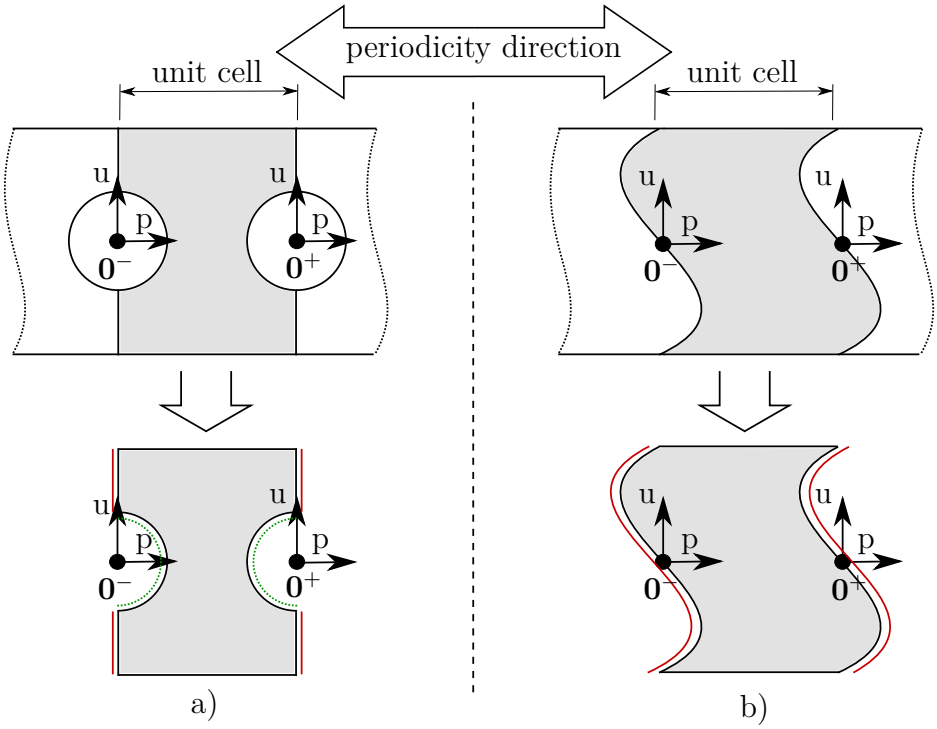

Figure 2.6.: Two scenarios for boundaries that differ from the control points in p-direction. Green (dotted line): no PBC , red (solid line): PBC

Nontrivial boundaries

Special care has to be taken in the case of boundaries that are not perpendicular to the direction of periodicity and/or uneven in the undeformed state. In the following, these boundaries that can also be specified by a non-constant local p-coordinate are termed *nontrivial boundaries*. For these nontrivial boundaries two possible types can be identified as depicted in Fig. 2.6 a) and b). In the case of Fig. 2.6 a) a void is modelled, meaning that a periodic arrangement is given but the requirement of parallelism between the corresponding boundaries is not met for all regions of the boundary. Due to the requirement of compatibility, only the parallel regions of the boundaries are subjected to PBC. Accordingly the boundaries in case of Fig. 2.6 b) are subjected to PBC without exception. For

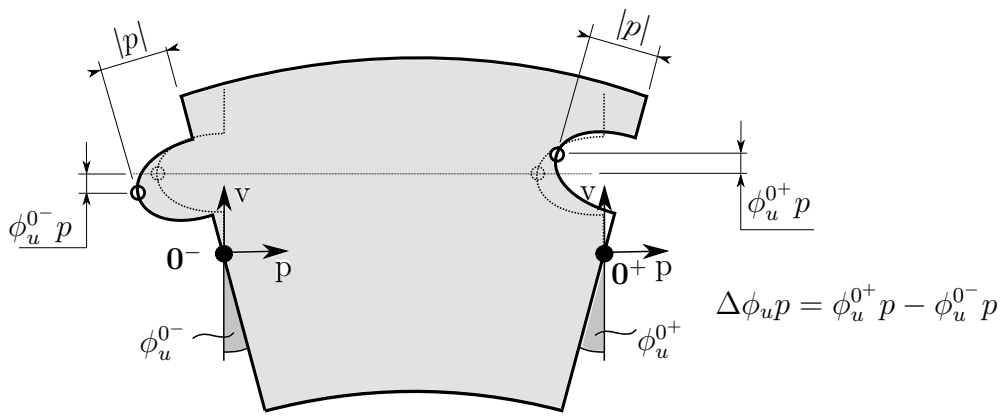

Figure 2.7.: Exemplary for bending about the u-axis: The contribution to the cross sectional displacement due to a difference in p-direction of the undeformed boundaries.

the bending load cases a difference in the p-coordinate of the boundaries results in a difference in the displacements b_u and b_v, see Fig 2.7. In consequence the kinematic coupling conditions, i.e. the PBC, cf. Eqs. (2.10)-(2.15), account for this behaviour by introducing the terms $\Delta\phi_v p$ and $\Delta\phi_u p$ in the equations for the displacement b_u and b_v Eqs. (2.10) and (2.11).

2.2. Variables in Postprocessing

Stiffness and strain energy

One of the main objectives of the presented uniaxial periodic unit cell approach is to gain the effective stiffness properties for the application to a larger scale. With the stiffness matrix, $\mathbf{S}$, the homogenised constitutive equation for the Euler-

Bernoulli-St-Venant beam can be put in the form,

$$\begin{bmatrix} F_p \\ M_u \\ M_v \\ M_p^t \end{bmatrix} = \begin{bmatrix} S_{11} & S_{12} & S_{13} & S_{14} \\ & S_{22} & S_{23} & S_{24} \\ & & S_{33} & S_{34} \\ symm & & & S_{44} \end{bmatrix} \begin{bmatrix} \langle \epsilon_p \rangle \\ \langle \chi_u \rangle \\ \langle \chi_v \rangle \\ \langle \chi_p \rangle \end{bmatrix} = \mathbf{S} \langle \bar{\epsilon} \rangle \quad , \tag{2.24}$$

where F_p and M_i denote the reaction force and reaction moments due to a displacement controlled loading. In correspondence to the four load cases, the vector $\langle \bar{\epsilon} \rangle$ is composed of the averaged extensional strain component $\langle \epsilon_p \rangle$ and the averaged curvature components $\langle \chi_i \rangle$ as,

$$\langle \bar{\epsilon} \rangle = \begin{bmatrix} \langle \epsilon_p \rangle \\ \langle \chi_u \rangle \\ \langle \chi_v \rangle \\ \langle \chi_p \rangle \end{bmatrix} = \frac{1}{l} \begin{bmatrix} \Delta b_p \\ \Delta \phi_u \\ \Delta \phi_v \\ \Delta \phi_p \end{bmatrix} \quad , \tag{2.25}$$

which can be expressed via the translational and rotational differences of the boundary faces with Eqs. (2.6)-(2.7). Cartraud et al. [5] and Dizy et al. [8] suggest a determination of the coefficients S_{ij} of the stiffness matrix on the basis of the strain energy per unit length. This scalar value is more comfortable to extract from the results file than the components of the reaction force or the reaction moment. The strain energy per unit length or the stiffness, respectively, constitute a suitable parameter for the verification of a unit cell simulation versus the simulation of the global structure as the energy has to be preserved over the scales (see section 2.1). The strain energy per unit length U^{lc} is calculated for every load case (superscript lc) as follows ([8]),

$$U^{lc} = \frac{1}{2} \langle \bar{\epsilon}^T \rangle \mathbf{S} \langle \bar{\epsilon} \rangle = \frac{1}{2l} \int_\Omega C_{ijkl} \epsilon_{ij} \epsilon_{kl} d\Omega \quad , \tag{2.26}$$

with C_{ijkl} denoting the material elasticity tensor and ϵ_{ij} denoting the small scale strain tensor for an integration over the volume of the unit cell Ω. The strain

energy per unit length U^{lc} resulting from each of the load cases is used to calculate the terms of the stiffness matrix in Eq. (2.24). In order to determine $\mathbf{S}$, ten load cases are needed, cf. appendix A:

- four displacement controlled load cases that represent pure tension, bending and torsion. These correspond to a single non-zero entry in the $\langle\bar{\epsilon}\rangle$ vector.
- six displacement controlled load cases that represent the possible pairwise superpositions of the abovementioned four.

For the diagonal terms,holds

$$S_{ii} = \frac{2U^{lc}}{\epsilon_i^2} \quad , \tag{2.27}$$

whereas the off diagonal terms are calculated as,

$$S_{ij} = \frac{2U^{lc} - (S_{ii}\epsilon_i^2 + S_{jj}\epsilon_j^2)}{2\epsilon_i\epsilon_j} \quad . \tag{2.28}$$

2.3. Nonlinear Effects

The presented approach is of elevated importance for computationally expensive simulations. FEM-Models incorporating nonlinear effects typically exhibit high computational demands due to their incremental solution technique. Thus it is important to know the potentials and limitations of the presented method with respect to nonlinear effects. In general, nonlinear behaviour is allowed to occur in the local model but has to result in an admissible solution meaning that the nonlinearity must occur periodically in the global structure. Dizy et al. [8] presented panel buckling in the cells of a ribbed beam as a relevant example. However, care should be exercised when examining unstable behaviour because the unit cell cannot represent instability modes on a larger scale than the unit cell such as e.g. the global column buckling in the case of the ribbed beam. In addition to periodic

nonlinear effects on the local scale, Dizy et al. [8] stated that geometrically nonlinear behaviour in the global model due to large deformations can still lead to sufficiently small deformations on the local scale and thus to the assumption of linear behaviour in the unit cell.

Furthermore nonlinearities in the constitutive law, relating strains and stresses, can be modelled with the help of a periodic unit cell. This nonlinearities manifest itself in e.g. plasticity or damage behaviour. Correspondingly, caution is advised because the assumption of periodicity has to be valid for every result. This means that e.g. in the case of delamination only the onset of damage can be simulated with the help of a periodic unit cell because considering damage propagation would lead to unphysical results as a periodic crack pattern is implied.

2.4. Torsion

This section aims to present the particularities of the torsional load case and the resulting limitations with respect to the presented method. As stated above, the presented approach assumes that *Saint Venant's Torsion* (SVT) governs the behaviour under a torsional load. SVT implicates that warping of the cross section is unconstrained and results in pure shear stress. Warping describes the existence of a displacement field of the cross section in direction of the beam axis. In contrast to the SVT, *Warping Torsion* describes a behaviour where warping is constrained e.g. by an encastered end resulting in shear stress plus normal stress.

This means that for the general case of constrained warping the presented homogenisation method is not applicable, as the effective properties cannot be represented accurately. However, Stegmair [22] denotes two exceptions for which the assumption of SVT holds regardless of constrained warping:

- SVT is a valid assumption for *warp free cross-sections* that are twisted

around its shear centre. A warp free cross-section is e.g. a closed circular section or a polygon section tangential to a circle. For more detailed consideration see e.g. [22].

- The warping deformation can be neglected for *thin walled closed profiles* and *solid sections* in most cases and the SVT is predominant. However, this assumption has to be verified for every case where the additional stress components due to warping torsion or the torsional stiffness, respectively, might play a decisive role.

3. Implementation

3.1. Programming of the PBC Generator

3.1.1. General remarks

The application of the PBC to an arbitrary model is realised by means of an automated modelling process, as the six Eqs. (2.10)-(2.15), cf. section 2.1, have to be implemented for every pair of corresponding nodes. This means that on the basis of the FEM-model of the unit cell, the PBC-generator has to generate a FEM model of the unit cell with PBC that can be analysed in a further step. Using Abaqus, there are two approaches:

- *Abaqus input file string manipulation*: The Abaqus input file contains the model information in text form and is designated to be solved by the Abaqus Solver. In this first approach the input file is read, evaluated and extended automatically regarding the PBCs by means of a Python algorithm. This method has the advantage that it can be applied independently from Abaqus CAE[1] to Abaqus input files generated in an arbitrary preprocessor.

- *Abaqus CAE model manipulation with the help of the scripting interface*: The Abaqus scripting interface for Python is an extension of the programming language Python, enabling the user to execute Abaqus commands in combination with a python algorithm to build or enhance a model. This advantage

[1] Abaqus CAE (**C**omplete **A**baqus **E**nvironment) is the 3-D interactive environment used to pre and post process FEM-model data.

> of using the Abaqus object library (i.e. the command toolset) entails an easy combination of the PBC generator with an automated model generator leading to the efficient modelling of parametric unit cell studies. Furthermore, the changes to the model can be verified visually in Abaqus CAE and a graphical user interface to input the necessary data is easy to realise.(*Abaqus Scripting User's Manual* and *Abaqus Scripting Reference Manual* [21])

In the present case the scripting interface method is used to realise the automated generation of PBC although the core algorithm is based on general python commands, meaning that the approach of using the input file can be implemented with some minor changes. Fig. 3.1 presents the concept of the PBC-Generator showing the basic sequence of operations, some of which are explained in more detail in the following sections.

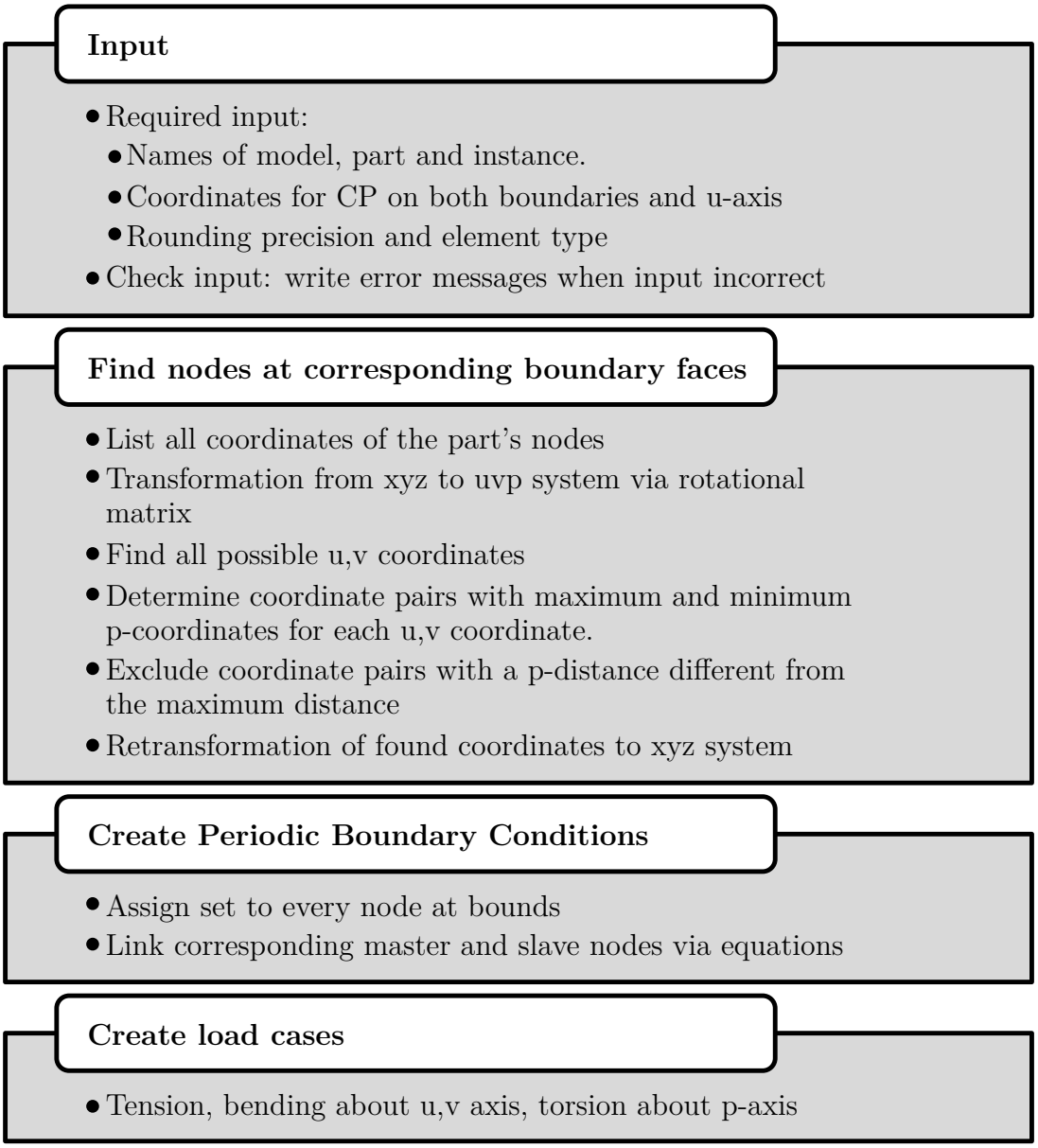

Figure 3.1.: Structure of algorithm that assigns PBC to an arbitrary uniaxial RUC model.

3.1.2. Model requirements and input

For an easy and intuitive input of the required data a RSG[2] was designed. A more detailed consideration of this RSG regarding its appearance and application is given in appendix A. By specifying the names of model, part and instance the generator is able to access the previously defined model information.

Nevertheless, the model of the unit cell has to possess the following properties for the generation of the PBC to work as designated:

- The geometry of the unit cell has to be suitable for a periodic arrangement (see section 2.1: requirement of compatibility). However, boundary faces f^+ and f^- with edges or faces parallel to the p-direction as well boundaries exhibiting undercuts (that are not due to an intersected void) are not suited for processing with the algorithm for boundary node determination.
- The mesh has to be defined in the part domain.
- The mesh must be conformal on the corresponding boundaries meaning the mesh on one face represents a projection along the direction of periodicity of the mesh on the other face.
- An instance for the part must be created.

Additionally, the axis of periodicity and the reference axis of the bending load cases have to be defined by specifying the control points on f^+ and f^- and the direction vector of the u-axis, respectively. The definition of the rounding precision denotes the decimal place after which the coordinate values are rounded. Rounding is important because especially for curved boundary shapes the nodes might not be completely coincident due to a numerical imprecision in the mesh generation. Care

[2]The **R**eally **S**imple **G**UI (**G**raphic **U**ser **I**nterface) is designed with a modular building tool in Abaqus-CAE

should be exercised as well when the model geometry is defined with decimal values smaller than 10^{-3}. A poorly chosen rounding precision might result in the omitting of a node pair for the generation of the PBC, that was conceived to be coincident. Deviating from the default value of six decimal places is only recommended if a visual check has shown that nodes have been omitted from the PBC generation and it is clear that the mesh is conformal to a sufficient degree. A selection between shell and volume elements refers to the element class the model boundaries are based on. In addition to that, the displacement values at the control points can be altered manually for example for a localisation approach. The rotations should not be chosen too large because geometrically nonlinear behaviour is not accounted for by the PBC (see section 2.1). The input is also submitted to a check and wrong or missing input is reported by an error message providing information how to correct the input error. See appendix A for a more detailed consideration of the model requirements and how the automated generator is operated correctly.

3.1.3. Algorithm to determine boundary nodes

The core aspect of the script is an algorithm that determines corresponding boundary nodes. The base data for this algorithm is a list of triples representing the coordinates of all nodes of the part given in the standard Abaqus coordinate system x, y, z. The basic idea is to find the nodes with minimum and maximum coordinate components in the direction of periodicity in order to determine the nodes that are part of the boundary faces. For this procedure to work, the nodal coordinates of an arbitrary model are transformed to the local u, v, p system where the direction of periodicity coincides with the p-direction. Thus, the lowest and the highest values in the p-direction represent the boundary faces. The change of base is realised by a three by three rotation matrix, $\mathbf{R}$, whose coefficients are calculated from three systems of linear equations linking the base vectors of the

x, y, z system to the ones of the u, v, p system. Hence, the position vector of every node, $\bar{n}_{uvp}$, is calculated from the original system as,

$$\bar{n}_{uvp} = \mathbf{R}\bar{n}_{xyz} \quad . \tag{3.1}$$

Having determined the minimum and maximum values leads to a list of corresponding node pair coordinates. From this list all pairs are excluded that do not exhibit the maximum distance between each other. This maximum distance equals the distance between the parallel faces f^+ and f^-. Without this elimination, node pairs from interior boundaries from e.g. a periodic perforation (see e.g. Fig. 2.6a)) are wrongly considered for the generation of PBC. Eventually, the node pair coordinates are retransformed to the original base via the inverted rotation matrix $\mathbf{R^{-1}}$.

3.1.4. Creating Periodic Boundary Conditions

The previous steps have determined the coordinates of all coincident node pairs on f^+ and f^-. The PBCs are now implemented with the help of the Abaqus `Equation` object (equivalent to the Abaqus `*EQUATION`-card in the input file) that defines a linear multipoint constraint between a set of degree of freedoms (see [21]) as,

$$A_1\lambda_i^P + A_2\lambda_j^Q + ... + A_N\lambda_k^R = 0 \quad , \tag{3.2}$$

where λ_i^P is the nodal variable at node P in DOF i and A_n are the coefficients that define the linear relation. Applied exemplarily to the present case for a node pair N^+ and N^- this leads for Eq. (2.10) to,

$$(-1)\lambda_u^{N^+} + (+1)\lambda_u^{N^-} + (-v)\lambda_{\phi^p}^{0^+} + (+v)\lambda_{\phi^p}^{0^-} + (+p)\lambda_{\phi^v}^{0^+} + (-p)\lambda_{\phi^v}^{0^-} = 0 \quad , \tag{3.3}$$

where e.g. $(-v)\lambda_{\phi^p}^{0^+}$ denotes the rotation ϕ^p of the control point 0^+ multiplied with the negative v-coordinate of the corresponding nodes N^+ and N^-.

In a last step the necessary load steps for the calculation of the effective properties (cf. section 2.2) are generated and the related displacements of the CPs are assigned. Ten general linear static load steps with automatic incrementation and a direct solving method are defined per default. See appendix A for a detailed listing of the ten load steps.

3.1.5. Automated Postprocessing

In addition to the automated generation of the PBC and the load cases a script has been conceived to evaluate the effective properties in the form of the stiffness matrix of model subjected to the presented uniaxial periodic loadcases, cf. Eq. (2.24). The script operates on the basis of the Abaqus output database and calculates the matrix entries as presented in section 2.2. See appendix A for a more detailed consideration of the required model configuration and information to run the script.

3.1.6. Performance of the algorithm

With regard to future applications of the presented method on large, highly resolved unit cell models, a time-efficient automated generator is essential. The computationally most demanding part of the algorithm is the determination of the boundary nodes, with the number of operations governing the calculation time. The number of operations is predominantly influenced by a number of comparisons between node coordinates where each node from a list l_1 of nodes is compared to each member of a node list l_2. The length of the lists $length(l_1) = f_1(n)$ and $length(l_2) = f_2(n)$ are functions of the total number of nodes n. Hence, the total number of comparisons $C = length(l_1) * length(l_2) = f_1(n) * f_2(n)$ shows a dependency of $C \sim n^2$. This can be roughly translated to a $T \sim n^2$ dependency for the total run time T of the generator. A first version of the algorithm showed satisfy-

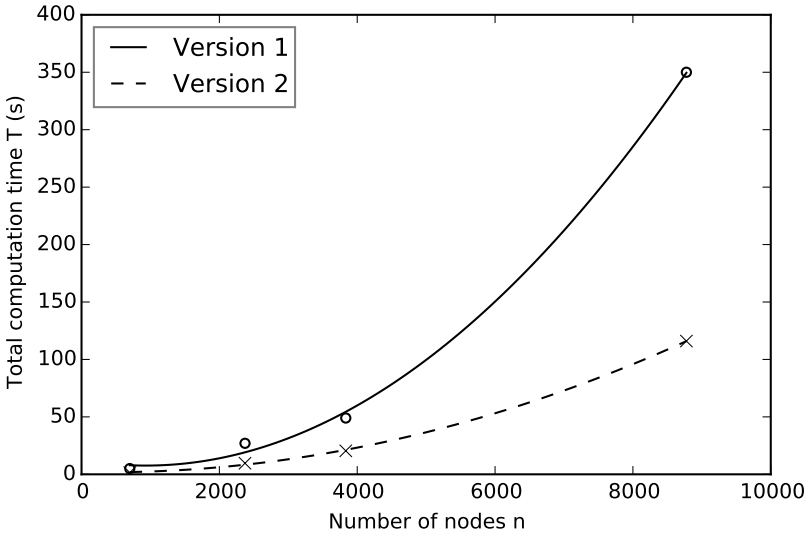

Figure 3.2.: Total run time of the algorithm over number of nodes: a comparison of the original algorithm (version 1 - solid line) and the optimised algorithm (version 2 - dashed line). The lines result from a quadratic regression.

ing performance for smaller models and models with entirely structured meshes, see Version 1 in Fig. 3.2. For a higher number of nodes the time for determining the boundary nodes turned out to question the practicability of the presented approach as it exerted the solving time for a long beam model.

In a second version of the algorithm the previously presented types of operations are optimised by reducing the length of lists l_1 and l_2 to a necessary minimum, see Version 2 in Fig. 3.2. This results in a significant improvement in total run time T. For a larger model with $n = 30000$ nodes, that are merely conformal at the periodic boundaries, the optimised algorithm takes about $T = 1000s$ to determine the boundary nodes and set up the PBC as well as the load cases.

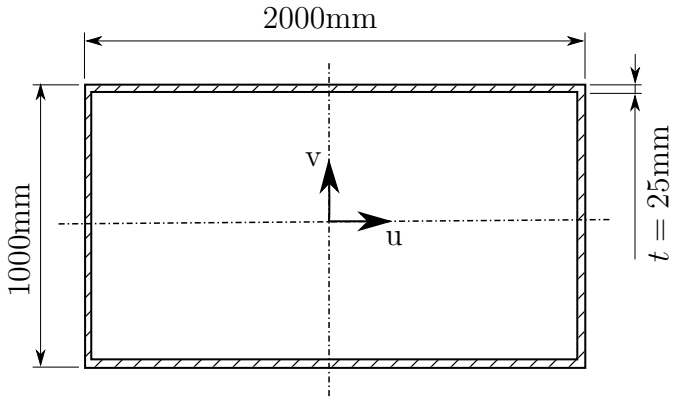

Figure 3.3.: Cross section of the prismatic box beam in accordance with Dizy et al. [8].

3.2. Examples for verification

In this section examples with different features are presented to verify the theoretical derivations and the resulting automated PBC generator. Reference solutions are given as well as a description of all model features that are not generated by the PBC generator. Thus, the definition of the unit cell according to the abovementioned requirements is described. In addition, rigid body modes must be prevented because in the present method the control points (CPs) are not part of the mesh and they merely express the difference in translational and rotational displacement of the corresponding faces. In order to prevent rigid body modes, mesh nodes of the respective unit cell model are constrained appropriately.

3.2.1. Example 1: Prismatic box beam

Dizy et al. [8] proposed a thin walled structure with a rectangular cross section (see Fig. 3.3) as a first reference for verification. Using isotropic, homogeneous material with a modulus, $E = 70.000\text{N/mm}^2$, and a poisson ratio, $\nu = 0.3$, this example is fairly basic. The length of the unit cell is $L = 1000\text{mm}$. Dizy et al.

[8] provide the following solution strategies for the diagonal components of the stiffness matrix:

- (I) the analytical solution from the thin walled beam theory,
- (II) the solution based on the periodic homogenisation approach presented in [8] modelled with volume elements,
- (III) the solution based on an alternative homogenisation approach using a variational asymptotic formulation, which was developed by Palacios et al. [19] and
- (IV) the solution of the long beam model based on volume elements.

In addition to these four reference solutions, the present work provides further solutions that are compared to the ones obtained in [8] in section 4.1.2. In total, four configurations (see Fig. 3.4) of the structure are modelled to verify different aspects of the presented approach:

- a) RUC with PBC based on volume elements (see Fig. 3.4 a)): This unit cell corresponds to the work of Dizy et al. [8] and aims to show the capability of the automated PBC generator to process volume elements. Four element layers represent the wall thickness.
- b) RUC with PBC based on shell elements (see Fig. 3.4 b)): The mesh fineness is equivalent to configuration a).
- c) RUC with PBC based on shell elements with nontrivial boundaries (see Fig. 3.4 c)): The boundaries exhibit two convex and two concave circular features of $R = 250$mm. The fine mesh accounts for an accurate representation of the circular shape.

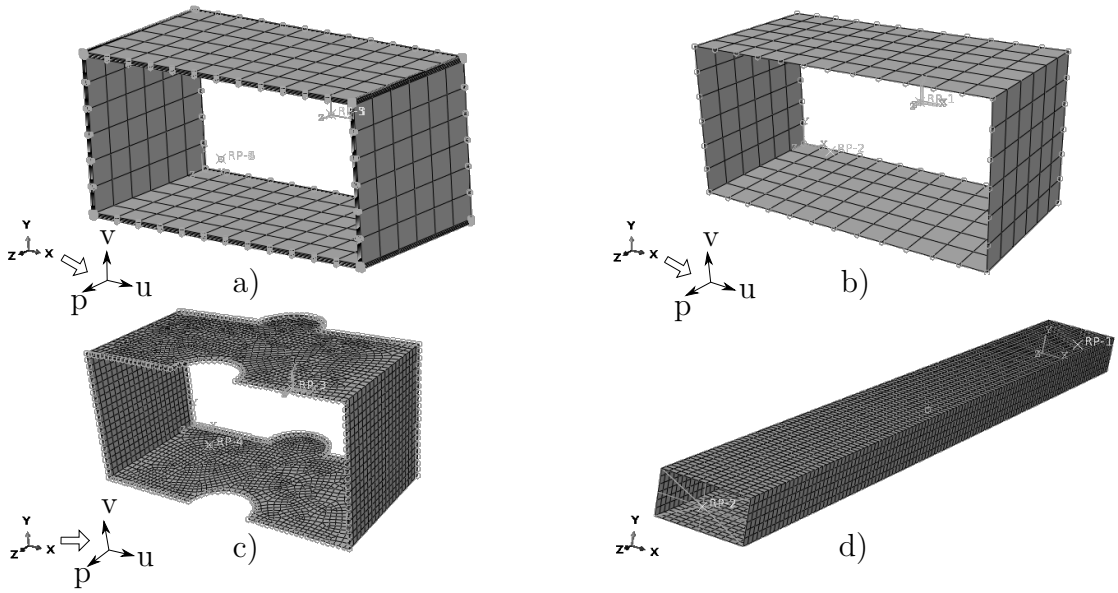

Figure 3.4.: Four configurations of the prismatic box beam depicting the mesh: a) RUC with PBC based on Volume Elements b) RUC with PBC based on shell elements c) RUC with PBC based on shell elements with nontrivial boundaries d) Long beam without PBC based on shell elements

- d) Long beam without PBC based on shell elements (see Fig. 3.4 d)): For the long beam the twentyfold length is chosen and the affine displacement values are applied via node-edge coupling on both ends. For the torsional load cases the coupling in p-direction is omitted to ensure warp free torsion. The element size is equivalent to configuration b).

Fully integrated elements with linear trial functions were used for both volume element model and shell element model. Rigid body movements were prevented by imposing appropriate boundary conditions on two nodes, centrally located on the side walls.

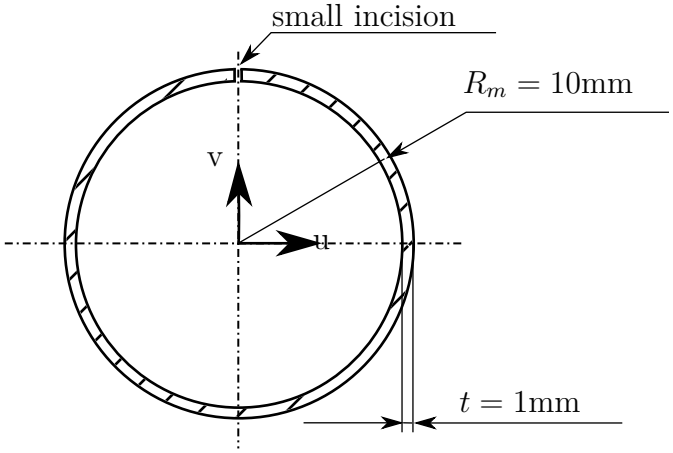

Figure 3.5.: Cross section of the thin walled open tube.

3.2.2. Example 2: Open circular cross section

This example aims to verify the free warping response of a RUC under PBC due to a torsional load. The cut circle was chosen as cross section (see Fig. 3.5) because it often serves as a typical example for open thin walled structures and an analytical solution for the torsional stiffness exists. An isotropic material with a modulus, $E = 210.000\text{N/mm}^2$, and a poisson ratio, $\nu = 0.3$, is modelled. The length of the unit cell is $L = 10$mm. In addition to the RUC model with PBC (see Fig. 3.6a)), a long tube with the ten-fold length and the same cross section serves as a reference model (see Fig. 3.6b)). In the case of the long model, affine displacement values are applied to the reference points that are coupled to the mesh edge. Again, the coupling in p-direction is omitted for the purely torsional load case. A mesh of fully integrated four-noded standard shell elements is employed exhibiting the same element size for both model configurations. The rigid body movement of the unit cell is prevented by subjecting 3 mesh nodes to the respective boundary conditions.

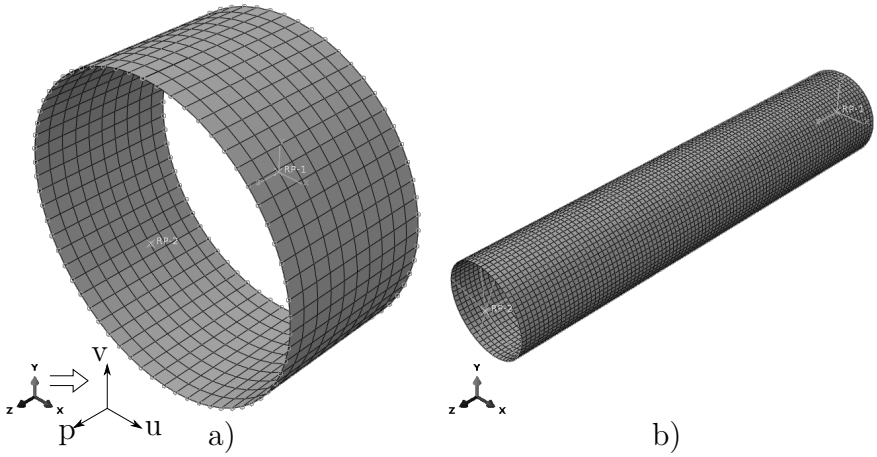

Figure 3.6.: The two shell model configurations of the thin walled open tube depicting the mesh: a) The RUC with PBC and b) the long tube with coupling constraints.

Analytical solution

As an additional reference, an analytical solution is provided. The diagonal elements of the stiffness matrix in Eq. (2.24) are calculated as:

- tensile stiffness: $S_{11} = EA$
- bending stiffness: $S_{22/33} = EI_i$
- torsional stiffness: $S_{44} = GI_t$

A defines the cross-sectional area; E and G denote the Young's modulus and the shear modulus, respectively. While the second moments of area I_i for the bending load cases are calculated straight forward according to the formula for a closed annulus, the torsional constant I_t for the open thin walled cross section is different from the torsional constant of a closed cross section. The theory for the torsion of a thin walled open cross section is based on the assumption that the open cross section can be treated as a plane plate under torsional load (see Fig. 3.7).

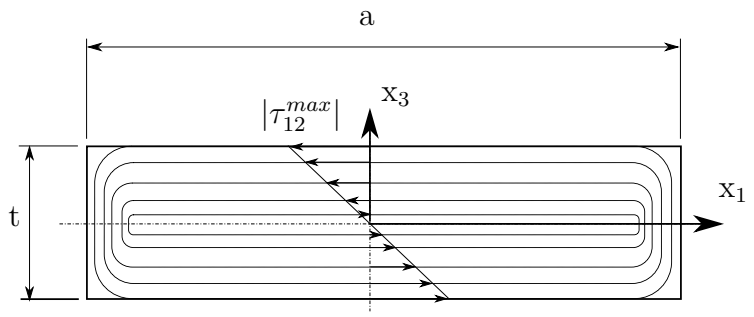

Figure 3.7.: Anti-metric shear stress distribution due to torsion of a plane plate as representation for an open thin walled cross section.

The coordinate system x_1, x_2, x_3 depicted in Fig. 3.7 represents a local coordinate system of a thin walled structure where the $x_1 - x_2$ plane equals a shear free neutral reference plane. According to Wiedmann [23] an anti-metric in-plane shear stress distribution $\tau_{12}(x_3)$ over the thickness of the plate t accounts for the torsional moment about the x_2-axis. This results in maximum negative and positive values of $|\tau_{12}^{max}|$ at the surfaces of the plate at $x_3 = +t/2$, $x_3 = -t/2$ and a zone of sign change at the edges $x_1 = +a/2$ and $x_1 = -a/2$. Neglecting these small zones of sign change leads to an approximated solution for the torsion of an open thin walled cross section (see e.g.[11]).

The torsional constant for an open thin walled cross section I_t is calculated with the wall thickness t and an integration over the accumulated length of the cross section a as,

$$I_t = \frac{1}{3} \int_a t^3 ds \quad . \tag{3.4}$$

However, this solution is based on the assumption of an non-curved neutral reference plane and represents an approximation for curved plates ([23]) which is the case for the present open circular cross section embodying a thin plate curved to

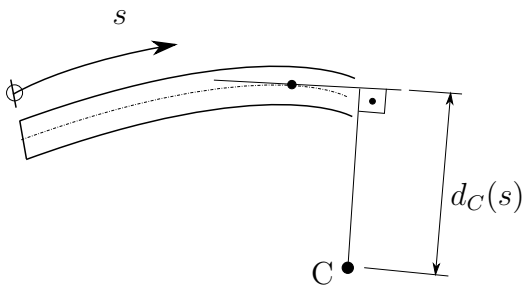

Figure 3.8.: Depiction of s-coordinate and distance definition according to [20].

a full circle. With the mean radius R_m, this leads for the present cross section to,

$$I_t \approx \frac{2}{3}\pi R_m t^3 \quad . \tag{3.5}$$

An approximation for the maximum absolute value of the shear stress is calculated analogously to the closed profile with the shear modulus G, the angle of twist $\Phi_p = \Delta\phi_p$ and the length l as,

$$|\tau_{12}^{max}| = \frac{Gt}{l}\Phi_p \quad . \tag{3.6}$$

Priebe [20] provides an analytical solution for the axial warping deformation u_w due to torsion about the centroid C of an arbitrary non warping free thin walled cross section as,

$$u_w = \zeta(s)\frac{d\theta}{dx_2} \quad , \tag{3.7}$$

where $\frac{d\theta}{dx_2}$ denotes the twisting in the abovementioned local coordinate system for a torsion with an angle of θ about the x_2-axis. With the distance $d_C(s)$ to the centroid the C, see Fig. 3.8, the unit warping $\zeta(s)$ is,

$$\zeta(s) = -\int_0^s d_C(s)\mathrm{ds} \quad , \tag{3.8}$$

for the torsion of symmetric profiles ([20]). For the present case the reference system of the warping deformation is chosen in the centre of the total circumference

so that the integration constant is zero. Hence, the axial warping deformation u_w of the open circular cross section for the case of the RUC is,

$$u_w = R_m \frac{\Delta\phi_p}{l} s \qquad with \quad -\pi R_m \leq s \leq +\pi R_m \quad , \tag{3.9}$$

which corresponds to a linear function $u_w(s)$.

3.2.3. Example 3: Perforated tube

This example represents a class of problems where the benefit of the presented approach is revealed. With the perforation constituting a periodic inhomogeneity the analytical solution is nontrivial and a highly resolved model of a long beam accounting for the induced strain and stress fields is computationally expensive. Thus, the effective properties gained from a periodic unit cell lead to an efficient modelling approach when applied to a large scale model. Regarding nonlinear behaviour this example is suited for the demonstration of periodically elastoplastic behaviour. With respect to the automated PBC generation and especially the algorithm determining the boundary nodes the chosen unit cell constitutes a good example to verify the correct implementation of PBC in case of nontrivial boundaries of the type depicted in Fig. 2.6 a). Figure 3.9 shows the periodic pattern of holes depicted on the flattened semicircle and how the smallest possible, strictly periodic unit cell is defined with a length of $L_{RUC} = 100\text{mm}$. The periodic pattern is applied to a steel ($E = 210.000\text{N/mm}^2; \nu = 0.3$) tube with a mean radius of $R_m = 100\text{mm}$ and wall thickness of $t = 5\text{mm}$. Analogously to the previously presented examples, a long tube with the tenfold length is modelled in order to verify the unit cell approach. Figs. 3.10 a) and b) show the resulting FE-Models. The size of the fully integrated four noded elements with linear trial functions is approximately the same for both models. The mesh of the RUC depicted in Fig. 3.10 consists of 2319 linearly elements. In addition to that, a second version

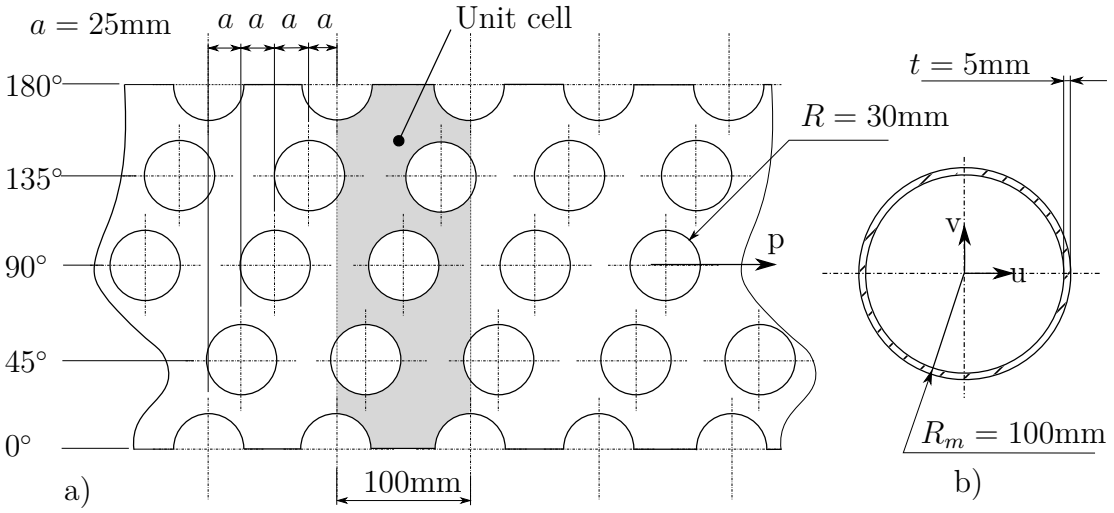

Figure 3.9.: Perforated tube: a) Flattened depiction of semicircle showing pattern and unit cell definition b) Cross section of the tube.

of the RUC with a mesh of 36293 elements was modelled in order to examine element size effects.

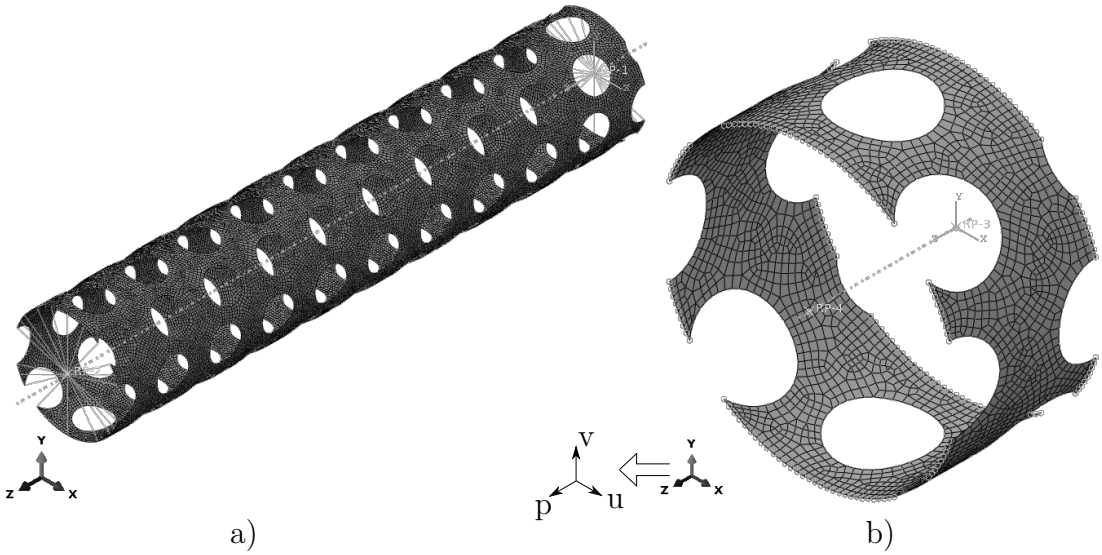

Figure 3.10.: FE Model of perforated tube: a) Long tube with coupling boundary conditions b) RUC with PBC.

Plasticity

In a second version of the model a nonlinear material law is applied in order to account for elasto-plastic material behaviour. For reasons of simplification isotropic linear elastic ideal plastic behaviour is modelled. The non-hardening behaviour is defined by a von Mises (J2) plasticity with a yield point at $\sigma_{\mathrm{Y}} = 500\mathrm{N/mm}^2$. This yield point is chosen arbitrarily with the only requirement being that plastic behaviour occurs for the load case under consideration. In order verify the results the RUC model and long tube model are simulated with the elastic ideal plastic material behaviour. The results exemplarily show the elasto-plastic behaviour of the perforated tube under tensile load.

4. Results and discussion

The results of all examples for verification are presented according to the following methodology: First, a component-wise consideration of the nodal displacements aims at verifying the geometric compatibility in the deformed state, cf. section 2.1. Secondly, the effective stiffness values of the unit cell model are compared to the ones of the large scale structure model and other reference solutions to assess the accuracy of the presented homogenisation approach. Thirdly, a comparison of the stress field of the unit cell and the corresponding large scale structure is given to evaluate the accuracy of stress field representation which is one of the basic requirements essential for both, localisation approach and homogenisation approach. The stress field is also analysed for continuity between the corresponding boundaries in the case of the unit cell model, cf. section 2.1. All results are discussed subsequent to their presentation in the respective sections. In addition to that, a specific conclusion regarding the abovementioned methodological steps is given.

4.1. Example 1: Prismatic box beam

4.1.1. Displacement

Using the example of the bending load case Fig. 4.1 shows a component-wise comparison of the displacement at the corresponding boundaries of the RUC faces, f^+ and f^-, as well as along a corresponding path of the long beam model. The path of the long beam model runs along the boundary of a segment in the centre of the

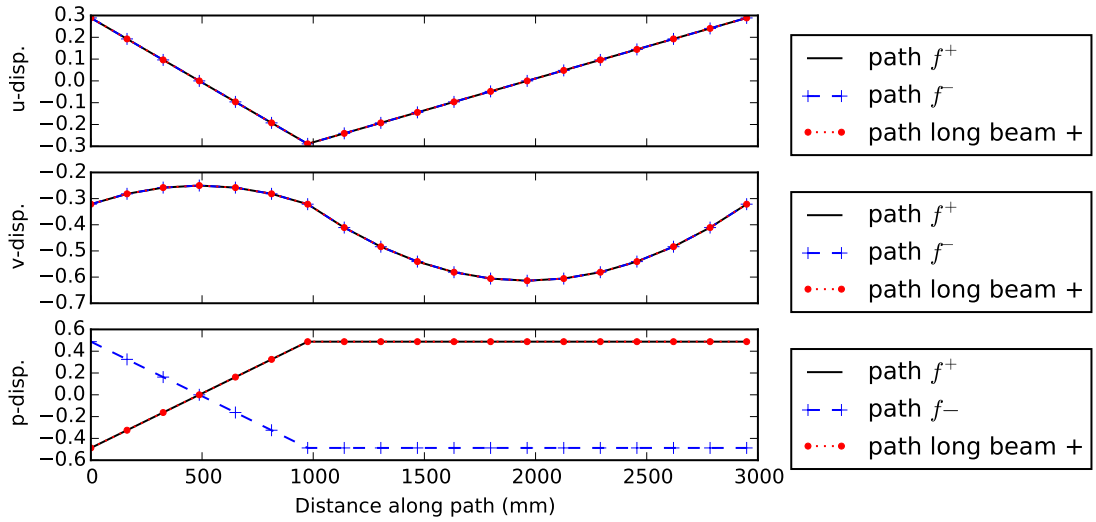

Figure 4.1.: Component-wise nodal displacements along the boundaries f^+ and f^- due to bending about the u-axis for the RUC based on shell elements (case b)). The plot paths and the coordinate system are defined according to Fig. 4.2. Values in mm.

long beam model which corresponds to the unit cell in dimension and loading, see Fig. 4.2. On one hand, the good agreement of the plots along the paths f^+ and f^- suggests that the unit cell is geometrically compatible to its fictitiously neighbouring unit cells in the deformed state. On the other hand, the good agreement of the RUC displacement with respect to the long beam displacement shows that the RUC with PBC gives a correct representation of the deformation state of a segment in the long structure. The v-displacement plot as well as the deformation of the different model configurations in Fig. 4.2 show that the PBC allow for an anticlastic curvature. This secondary deformation phenomenon is caused by the poisson effect and describes an additional curvature of the box walls about the p-axis due to bending about the u-axis.

4.1.2. Stiffness

The stiffness matrix,

$$\mathbf{S} = \begin{bmatrix} 1.032 * 10^{10} & 0 & 0 & 0 \\ 0 & 1.913 * 10^{15} & -6.25 * 10^{7} & 0 \\ 0 & -6.25 * 10^{7} & 5.575 * 10^{15} & 6.25 * 10^{7} \\ 0 & 0 & 6.25 * 10^{7} & 1.693 * 10^{15} \end{bmatrix} , \tag{4.1}$$

exemplarily shows for the standard RUC with shell elements (case b)) how the stiffness matrix is composed of values in the N-mm unit system. All off-diagonal terms are either zero or negligible due to their relative order of magnitude. This holds true for all model configurations a) b) c) and d). Thus, Tab. 4.1 compares the diagonal stiffness terms resulting from the four model configurations of the present work to the results presented by Dizy et al. [8]. The results in Tab. 4.1 show good agreement among one another as well as compared to the results of Dizy et al. [8]. It is noteworthy that the standard RUC stiffness values (case b)) agree very well with the ones of the RUC with nontrivial boundaries (n.t.b.) (case c)). The diagonal terms are equal at least up to the fourth significant digit. This indicates, that the supplementary terms $\Delta\phi_v p$ and $\Delta\phi_u p$ in the PBC account correctly for nontrivial boundaries (see section 2.1). The slightly higher deviation of the volume element RUC (case a)) for the bending load cases (relative deviation $< 0.5\%$) in comparison to the results of Dizy et al. [8] can be attributed to a different strategy for the application of the boundary conditions responsible for the unit cell curvature, see section 2.1. Hence, the presented method yields a reliable tool for the determination of the effective properties of a prismatic box beam. All in all, considering the first four significant digits of the results of the four model configurations in the present work, the relative deviation does not exceed 0.25 percent.

Table 4.1.: Diagonal elements of stiffness matrix for the prismatic box beam

	Present work				Dizy et al. [8]			
case (Fig.3.4)	a)	b)	c)	d)	I	II	III	IV
elements configuration	Vol. RUC	Shell RUC	Shell RUC n.t.b.	Shell Long beam	- Analyt. sol.	Vol. RUC	- UM / VABS	Vol. Long beam
$S_{11}(10^9\text{N})$	10.3	10.3	10.3	10.3	10.3	10.3	10.3	10.3
$S_{22}(10^{15}\text{Nmm}^2)$	1.91	1.91	1.91	1.92	1.91	1.91	1.91	1.91
$S_{33}(10^{15}\text{Nmm}^2)$	5.56	5.58	5.58	5.58	5.58	5.58	5.58	5.58
$S_{44}(10^{15}\text{Nmm}^2)$	1.71	1.69	1.69	1.70	1.79	1.71	1.71	1.71

4.1.3. Stress

The averaged stress results of the FE simulation suggest that the stress field is continuous at the periodic boundary faces and nearly identical in distribution and magnitude for the different model configurations and for all load cases under consideration. Since the box beam does not exhibit any inhomogeneities the strains and stresses are constant in p-direction. Exemplary for the load case of pure bending about the u-axis Fig. 4.2 shows a comparison of the maximum principal stress contours. The consideration of the maximum principal stress allows a comparison of the tensile stress due to bending of the four model configurations where the reference systems for the stress components is different for volume and shell elements as well as on the different faces of the shell element model. Figure 4.3 shows a linear stress progression over the length of the side faces in all four cases. This is in accordance with the well known linear tensile-compressive stress distri-

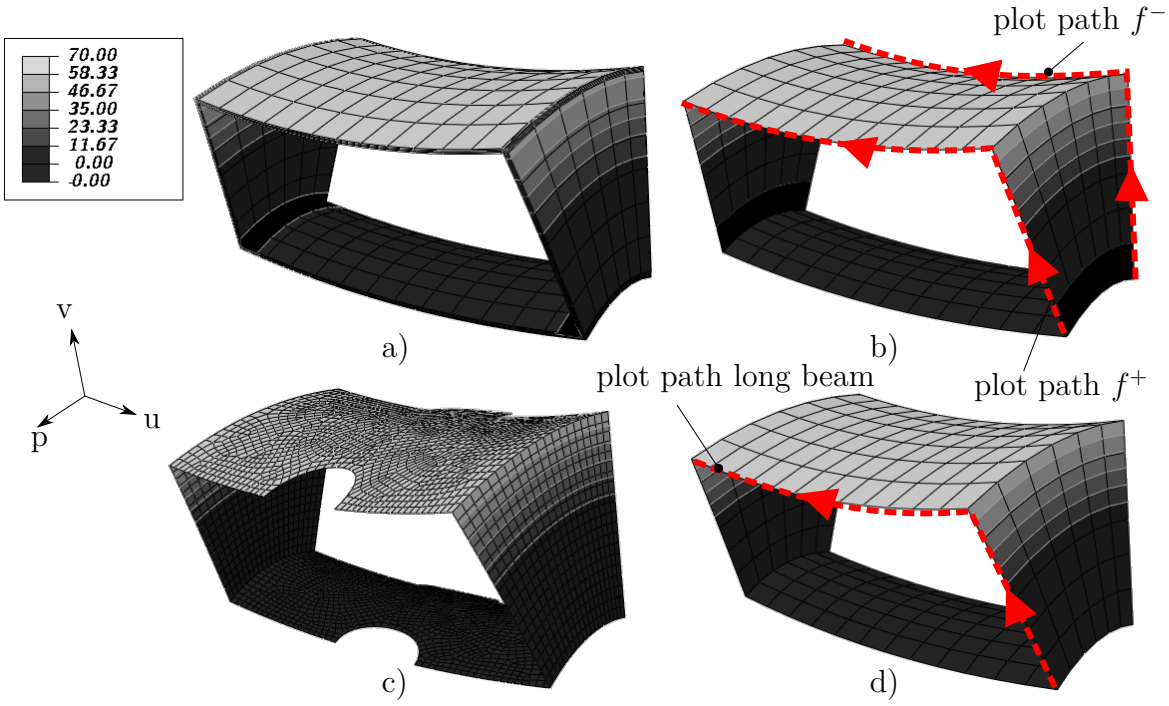

Figure 4.2.: Contour plot of maximum principle stress for bending about the u-axis: a) RUC based on volume elements b) RUC based on shell elements c) RUC with nontrivial boundaries d) Segment depiction from the long beam model. The deformation is depicted 200-fold magnified and stress values are in N/mm^2.

bution due to bending. In addition to that, the constant maximum values at the top face show very good agreement, cf. Tab. 4.2. Tab. 4.2 lists a comparison of characteristic stress values rounded to four significant digits for the four model configurations. The stress values for the shell element models are evaluated at the respective outer section point and for the volume elements at the outer integration points of the outer element. The slightly lower stress for the bending load cases of the volume element model (case a)) is attributed to this difference of evaluation position, meaning that the volume element's integration point is not exactly on the face of the respective wall. The slight deviation of the maximum principle stress

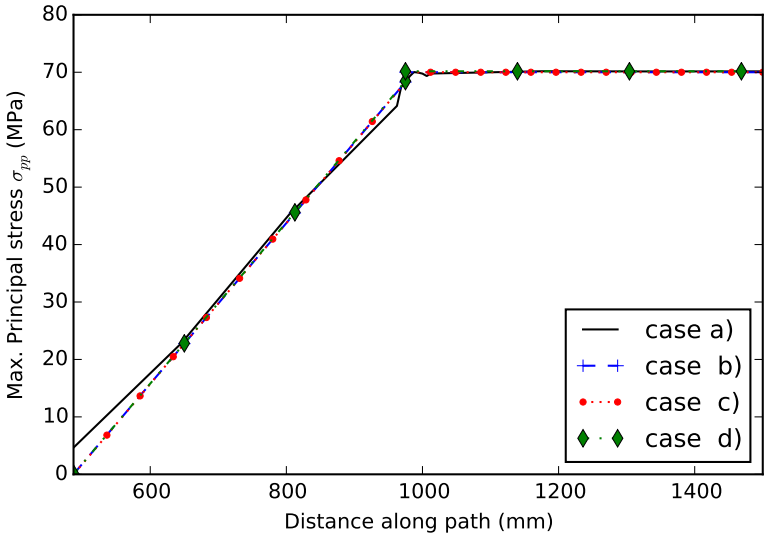

Figure 4.3.: Maximum principle stress over a segment of the path for all configurations presented in Fig. 4.2. The depicted segment of the plot path equals a path from the centre of the side wall to the centre of the top wall.

in case of the volume element model at the centre of the side wall as well as on the edge of side and top wall may be attributed to a shear locking effect, see solid line in Fig. 4.3. Since the shear stress due to torsion underlies small fluctuations because of a discontinuous jump from τ_t to $-\tau_\mathrm{t}$ at the edges between two faces, Tab. 4.2 shows the averaged value as an approximation for the nearly constant absolute value of the shear stress on the faces. According to the coordinate system depicted in Fig. 4.2 the absolute value of the shear stress $|\tau|$ in Tab. 4.2 corresponds to the shear stress $|\tau_{up}|$ on the top and bottom wall and to the shear stress $|\tau_{vp}|$ on the side walls, respectively.

Table 4.2.: Stress components of specific load cases in comparison for different modelling approaches.

	Present work. All results in N/mm^2			
case	a)	b)	c)	d)
elements	Vol.	Shell	Shell	Shell
configuration	RUC	RUC	RUC n.t.b.	Long beam
Tension: const. σ_{pp}	14.00	14.00	14.00	14.03
Bend u: max. σ_{pp}	69.56	70.00	70.00	70.17
Bend v: max. σ_{pp}	139.6	140.0	140.0	140.2
Torsion: const.$\lvert\tau\rvert$	$\approx$36.5	$\approx$36.5	$\approx$36.5	$\approx$36.5

4.2. Example 2: Open circular cross section

4.2.1. Displacement

Fig. 4.4 exemplarily shows for the torsional load case a component-wise comparison of the displacement at the corresponding boundaries of the RUC, f^+ and f^-, as well as along a corresponding path of the long beam model. The components are expressed with reference to a cylindrical r, θ, z coordinate system as depicted in Fig. 4.5. A good agreement of the displacement field at the corresponding boundaries as well as with a corresponding path of the long tube model is shown. This leads to the conclusion that the deformed unit cell is compatible to its fictitiously neighbouring unit cells and that the RUC correctly represents the deformation of a segment of the long tube model. The constant difference in θ-displacement between the corresponding faces f^+ and f^- is in accordance with the difference in displacement introduced via the control points. The displacement in z-direction

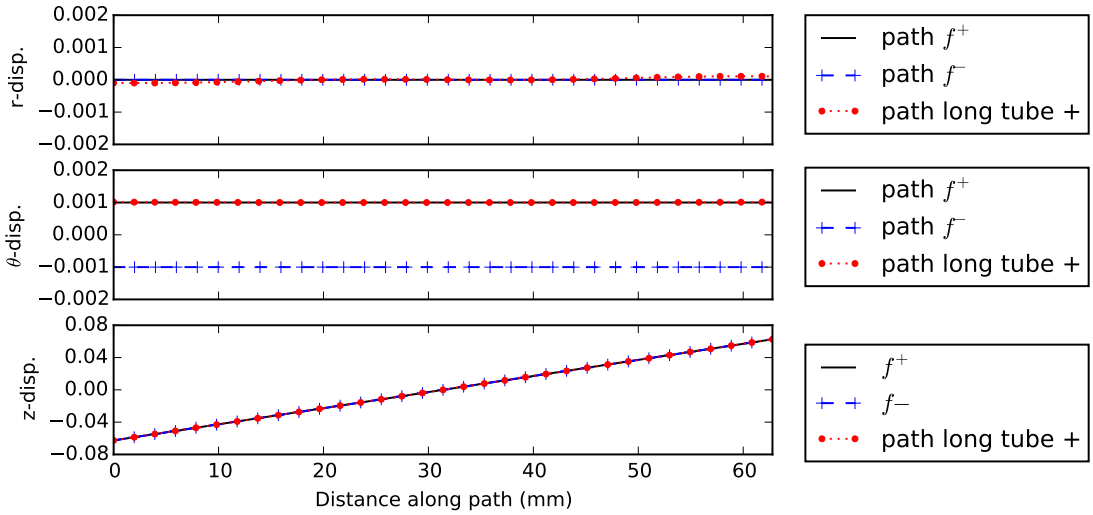

Figure 4.4.: Component-wise displacement due to torsional load along the corresponding boundaries f^+ and f^- as well as along a respective path of the long tube model. The plot paths and the cylindrical r, θ, z reference system are defined according to Fig. 4.2 and the displacement is given in mm.

(direction of periodicity) exhibits for both RUC model and long tube model a linear behaviour which is in accordance with the analytical results in section 3.2.2. The analytical solution suggests a linear dependency of the warping deformation u_w to the circumferential coordinate s with a slope of $m_{analyt} = R_m \frac{\Delta\phi_p}{l} = 2 * 10^{-3}$mm. The curve of the axial warping deformation gained from the FEM-results (see Fig. 4.4) exhibits a slope of $m_{FEM} = 1.96 * 10^{-3}$mm, showing good agreement to the analytical results.

4.2.2. Stiffness

The stiffness matrix,

$$\mathbf{S} = \begin{bmatrix} 1.319 * 10^7 & -3.790 * 10^4 & -2.529 * 10^2 & 1.184 * 10^1 \\ -3.790 * 10^4 & 6.580 * 10^8 & -2.441 * 10^3 & -1.743 * 10^1 \\ -2.529 * 10^2 & -2.441 * 10^3 & 6.584 * 10^8 & 2.071 * 10^1 \\ 1.184 * 10^1 & -1.743 * 10^1 & 2.071 * 10^1 & 1.657 * 10^6 \end{bmatrix} , \tag{4.2}$$

exemplarily shows for the standard RUC with shell elements (case a)) how the stiffness matrix is composed of values in the N-mm unit system. Most of the off-diagonal terms are negligible due to their relative order of magnitude. Solely, the matrix entries S_{12} and S_{21}, respectively, show relatively high values that cannot completely be neglected, suggesting a coupling of tensile and bending stiffness about the u-axis. This is attributed to the fact that the small incision causes a small shift of the centroid of the cross sectional area away from the u-axis which is defined by the position of the control points. Thus, the position of the control points is essential for the evaluation of the structural stiffness. In other words, a consideration of the whole stiffness matrix is necessary for a homogenisation approach when non-negligible off-diagonal terms suggest a coupling between the four principle stiffnesses.

A comparison of the RUC model, the long tube model and the analytical solution is presented in Tab. 4.3, showing four significant digits of the stiffness constants. The tensile stiffness values as well as the bending stiffness values show good agreement among the three solution strategies, meaning that a relative deviation of under one percent between the maximum and the minimum value is observed. The slight difference in bending stiffness about u and v axis is accredited to the non-zero thickness of the longitudinal cut which is not taken into account for the analytical solution of the bending stiffness. Solely the torsional stiffness values show a slightly higher relative deviation of approximately two percent which is

Table 4.3.: Diagonal entries of the stiffness matrix for the open circular cross section

	Present work		
case	a)	b)	c)
elements configuration	Shell RUC	Shell Long tube	- Analyt. solution
$S_{11}(10^6\text{N})$	13.19	13.24	13.19
$S_{22}(10^6\text{Nmm}^2)$	658.0	660.2	659.7
$S_{33}(10^6\text{Nmm}^2)$	658.4	661.0	659.7
$S_{44}(10^6\text{Nmm}^2)$	1.657	1.661	1.692

attributed to the fact that the analytical solution represents an approximation, see section 3.2.2.

Consequently, the RUC approach with the presented PBC is seen as an adequate method for the determination of the effective stiffness properties of the open circular cross section. In the case of the torsional stiffness of an open thin walled cross section, the correct kinematic modelling of the free warping deformation mode is essential (see Fig. 4.3). Thus, the good agreement of the torsional stiffness values leads to the conclusion that the PBC provide a correct kinematic coupling of the corresponding boundaries regarding free warping deformation.

4.2.3. Stress

Fig. 4.5 shows a contour plot of the shear stress and a magnified depiction of the deformation due to a torsional load. The depicted paths serve as the basis for a detailed comparison of the RUC model and the long tube model regarding stress

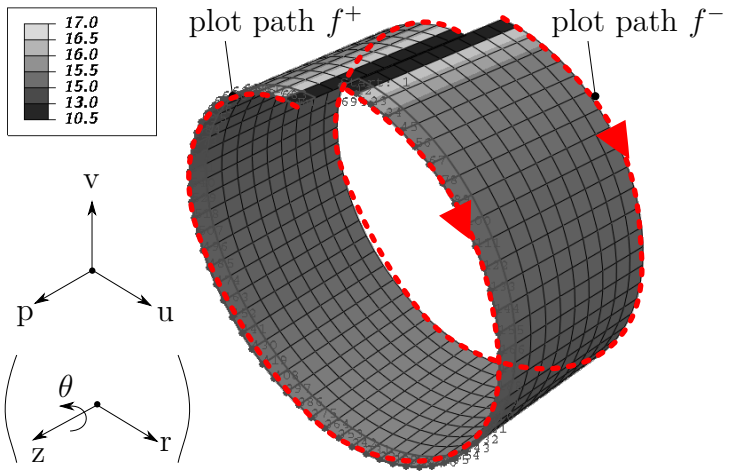

Figure 4.5.: Contour plot of torsional shear stress $|\tau_{\theta z}^{max}|$ of the RUC with 20-fold magnified depiction of the deformation. The dashed lines represent the paths for the plots in Fig. 4.4 and Fig. 4.6. Values in the legend are in N/mm^2.

and deformation, see Fig. 4.4 and Fig. 4.6. The FEM-stress results in Tab. 4.4 regarding tension and bending are evaluated at the outer section points of the shell element models. The results show good agreement with the analytical stress results for the tension and bending load cases for both model configurations.

The maximum shear stress $|\tau_{\theta z}^{max}|$ corresponds to σ_{12} at the outer section point in the shell element reference system. According to the theory presented in section 3.2.2 the values of maximum shear stress are evaluated far from the zones of sign change in the area where a constant shear stress over the circumference is expected. In this area the RUC model exhibits a constant shear stress value along the circumference of the cross section, see Fig. 4.6. The long tube model, however, shows a small, wavelike fluctuation of the shear stress with an amplitude of approx 0.3 N/mm^2. In order to compare this value to the other results, an averaged value is determined for the area of this wavelike fluctuation (represented by the blue

Table 4.4.: Stress components for specific load cases in comparison for different modelling approaches. * averaged value.

	Present work. All results in N/mm^2		
code	a)	b)	c)
elements configuration	Vol. RUC	Shell Long tube	- analyt. sol.
Tension: const. σ_{pp}	4200	4215	4200
Bend u: max. σ_{pp}	439.9	441.0	441.0
Bend v: max. σ_{pp}	439.7	441.5	441.0
Torsion: const. $\lvert\tau_{\theta \mathrm{z}}^{\max}\rvert$	16.20	16.53*	16.15

dotted line in Fig. 4.6). The relative deviation of this averaged value regarding the result of the RUC model is approximately two percent. This deviation as well as the wavelike fluctuation may be ascribed to load application effects that are not completely faded away.

The graph of the shear stress in Fig. 4.6 exhibits a discontinuous jump in the abovementioned zones of sign change at the edges of the longitudinal cut and a minimum value at the edges of approximately 10.5 N/mm^2. This is attributed to the inability of a shell element model to adequately represent the shear stress distribution in these zones which leads to unphysical results. Consequently, an alternative local mesh size may yield significantly different results.

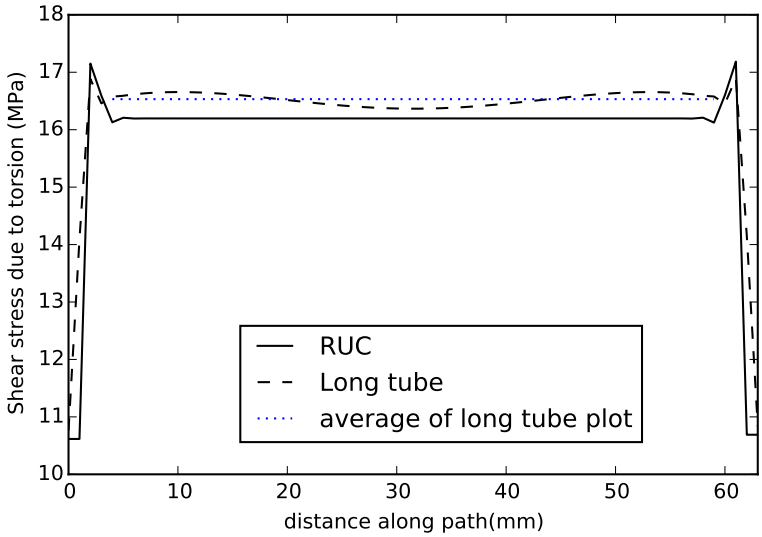

Figure 4.6.: Plot of the maximum shear stress $\tau_{\theta z}^{max}$ for the RUC (solid line) and the long tube model (dashed line). The blue dotted line represents the averaged value of the wavelike fluctuation of the long tube shear stress. The curves are plotted along the path f^+ as defined in Fig. 4.5.

4.3. Example 3: Perforated tube

4.3.1. Displacement

Fig. 4.7 exemplarily shows for the torsional load case a component-wise comparison of the nodal displacements at the corresponding boundaries of the RUC, f^+ and f^-. The components are expressed with reference to a cylindrical r, θ, z coordinate system as depicted in Fig. 4.8. A good agreement between the displacement of the corresponding boundaries can be observed in the case of the r-displacement. The same holds true for the θ-displacement which shows a constant difference corresponding to the rotational difference at the control points providing the dis-

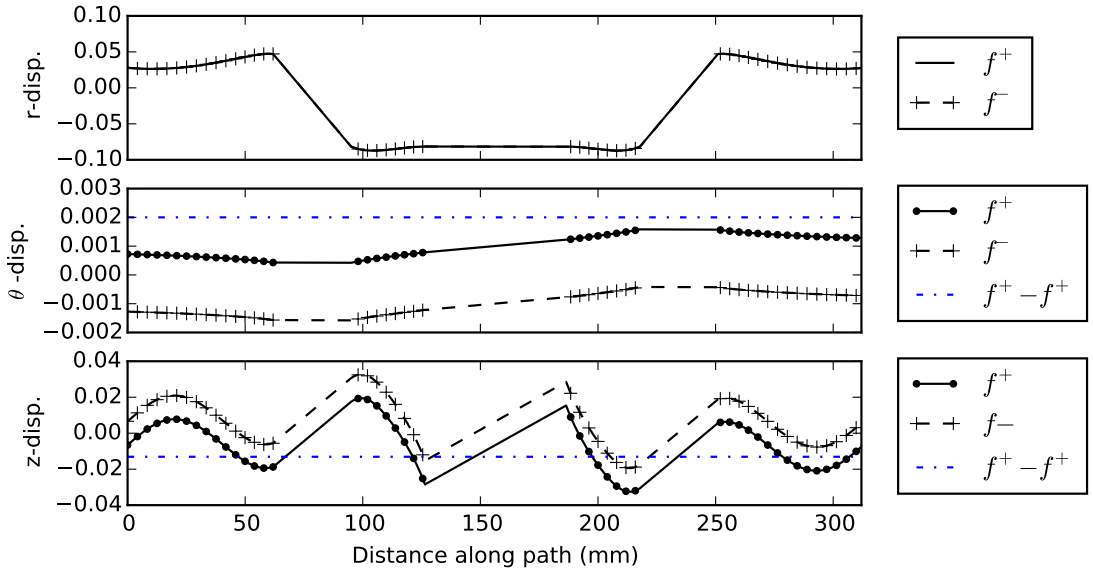

Figure 4.7.: Component-wise nodal displacements due to torsional load in cylindrical r-θ-z system at the corresponding boundaries f^+ and f^-. The plot paths are defined according to Fig. 4.8.

placement controlled torsional load application. The plot of the z-displacement shows two parallel curves suggesting the presence of a periodic strain microfield in periodic direction. The congruence and the constant difference of the curves, respectively, lead to the conclusion that the deformed unit cell is geometrically compatible to its fictitiously neighbouring unit cells.

4.3.2. Stiffness

The stiffness matrix,

$$\mathbf{S} = \begin{bmatrix} 2.232 * 10^{08} & -3.730 * 10^{05} & 1.043 * 10^{06} & 1.449 * 10^{09} \\ -3.730 * 10^{05} & 1.113 * 10^{12} & 5.355 * 10^{08} & 4.905 * 10^{07} \\ 1.043 * 10^{06} & 5.355 * 10^{08} & 1.100 * 10^{12} & 1.269 * 10^{08} \\ 1.449 * 10^{09} & 4.905 * 10^{07} & 1.269 * 10^{08} & 5.249 * 10^{11} \end{bmatrix} , \tag{4.3}$$

Table 4.5.: Diagonal elements of the stiffness matrix of the perforated tube

	Present work	
case	a)	b)
elements configuration	Shell RUC	Shell Long tube
$S_{11}(10^6\text{N})$	223.2	224.4
$S_{22}(10^{12}\text{Nmm}^2)$	1.113	1.111
$S_{33}(10^{12}\text{Nmm}^2)$	1.100	1.109
$S_{44}(10^{12}\text{Nmm}^2)$	0.5249	0.5109

exemplarily shows for the standard RUC with shell elements how the stiffness matrix is composed of values in the N-mm unit system. Again, some of the off-diagonal terms show a slight coupling of the principal stiffnesses.

A comparison of the RUC model and the long tube model is presented in Tab. 4.5, showing the first four significant digits of the relevant stiffness constants. The results for the tensile and bending load cases show good agreement with a relative deviation among the model configurations of under one percent. A relative deviation of under two percent for the torsional load case is rated as acceptable.

The good agreement of the RUC model and the long tube model suggests that the presented method provides an adequate solution for a homogenisation approach.

4.3.3. Stress

The stress field is exemplarily examined for the torsional load case. Fig. 4.8 depicts a contour plot of the in-plane shear stress as a key stress component for this load

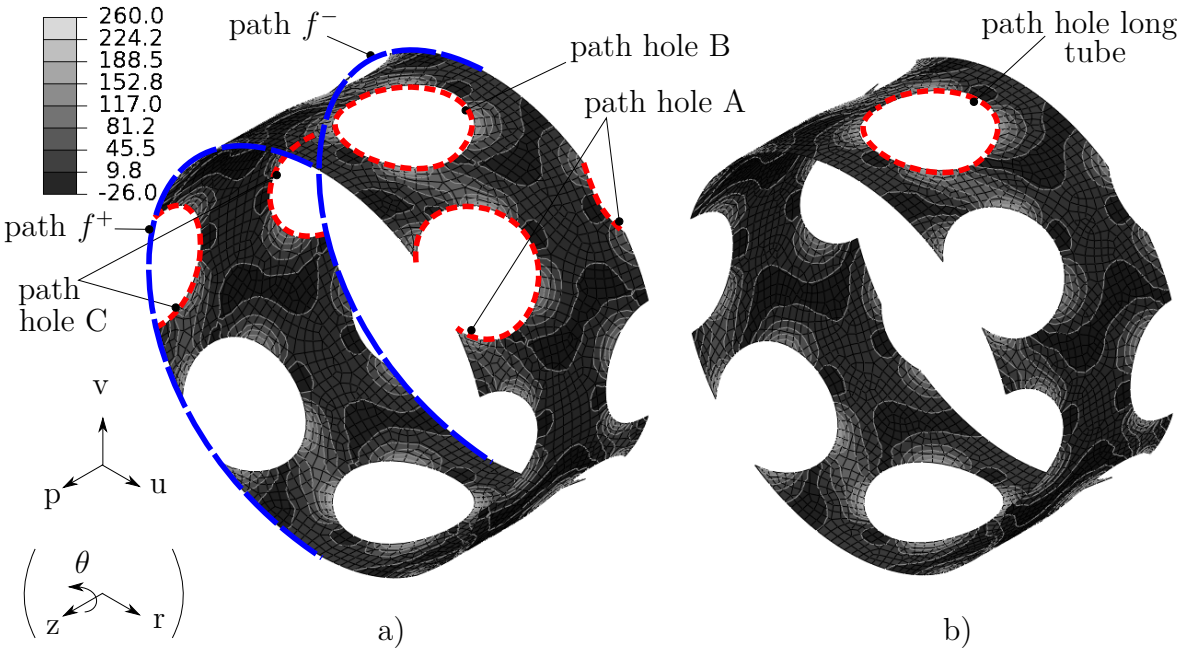

Figure 4.8.: Contour plot of the in-plane shear stress $\sigma_{\theta z}$ due to torsional load: a) RUC model and b) segment of the long tube model. Values in the legend are in N/mm^2.

case. Furthermore Fig. 4.8 shows how various paths are defined that serve as the basis for the following curve charts. In order to examine the shear stress field Fig. 4.9 shows a comparison of a periodic arrangement of unit cells (Fig. 4.9 a)) and a segment of the long tube model (Fig. 4.9 b)). The stress field of the RUC shows good agreement to the one of the long tube model. However, a close look at the boundaries of the RUC in Fig. 4.9 a) reveals that the averaged stress field shows a slight discontinuity. This discontinuity can also be observed for the other stress components as e.g. σ_{zz} ($=\sigma_{pp}$) in Fig. 4.10. Fig. 4.10 represents a curve plot along the paths f^+ and f^- (see Fig. 4.8) and the corresponding path of the long tube model. In particular the boundary regions close to the hole edges show a difference for the stress extrapolated to the nodes when comparing the different

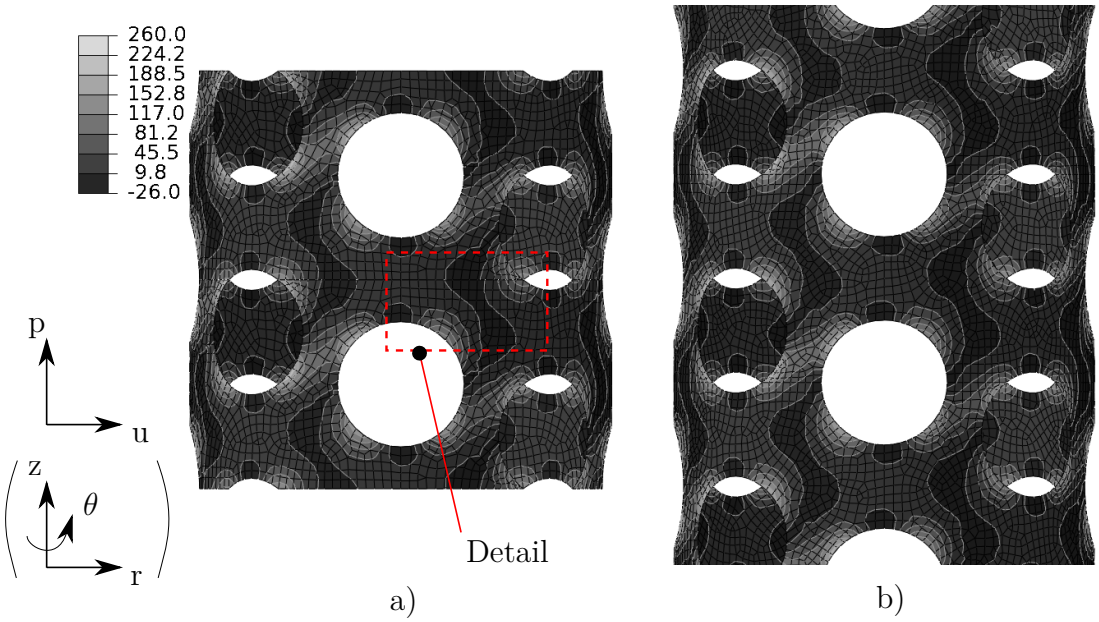

Figure 4.9.: Shear stress $\sigma_{\theta z}$ due to torsion for a) twofold depiction of the RUC b) a depicted segment of the long tube model. The detail is depicted in Fig. 4.11 for different mesh sizes.

paths.

This discontinuity of the averaged stress field is attributed to the missing averaging link between the integration points at the corresponding boundaries which is particularly influential in regions with a high stress gradient close to the boundary. An alternate, non-standard post-processing could provide an averaging link for the stress results at the integration points. In addition to that, the inadequately sharp element angles at the sharp hole edges cause poor results. In order to demonstrate how these peculiarities of the displacement based FEM and its standard post-processing cause this discontinuity, a model with a refined mesh is simulated, which reduces the nominal distance between the integration points at the corresponding boundaries and improves the mesh quality at the sharp edges.

This refined model (see Fig. 4.11 b)) yields better results in terms of quasi

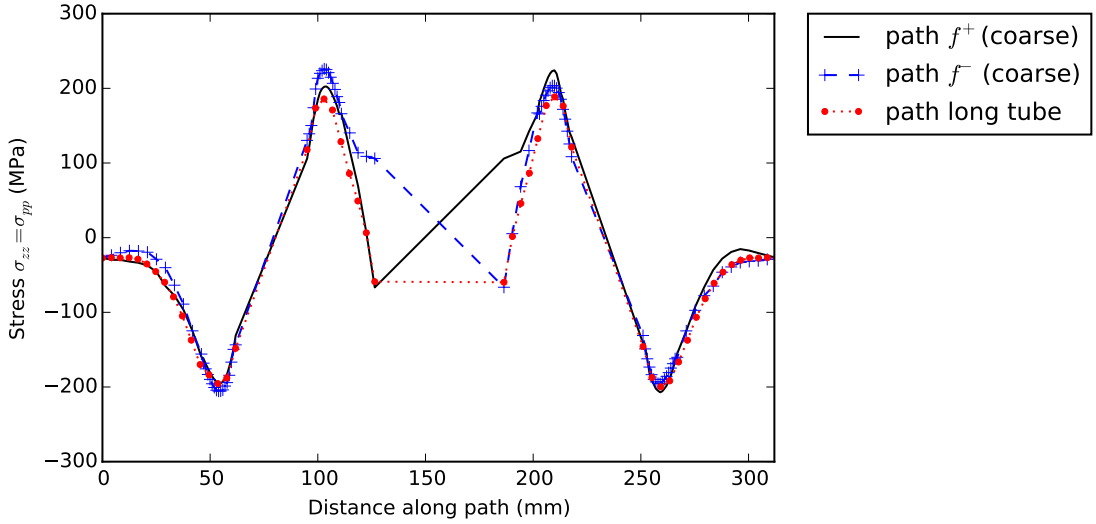

Figure 4.10.: Stress component σ_{zz} (σ_{pp}) along circumferential paths of the RUC with a coarse mesh and the long tube model, see Fig. 4.8 for the definition of the hole paths.

continuity between the corresponding boundaries and in comparison to the long tube model. Fig. 4.11 depicts a comparison of the shear stress field for the coarse mesh model and the model with refined mesh. The averaged stress field in this detailed view of the boundary region between two neighbouring unit cells RUC^i and RUC^{i+1} (see Fig. 4.9) exhibits a significant improvement for the refined mesh regarding its stress continuity at the boundaries. Additionally, Fig. 4.12 shows all relevant stress components for the RUC model with refined mesh. The improved agreement of the corresponding curves gives evidence of the described effects. However, in the boundary regions of the intersected hole edges, the curves of the stress components still show a slight deviation for the different paths. This local deviation is rated as acceptable and attributed to the described peculiarities of the displacement based FEM and its standard post-processing, respectively.

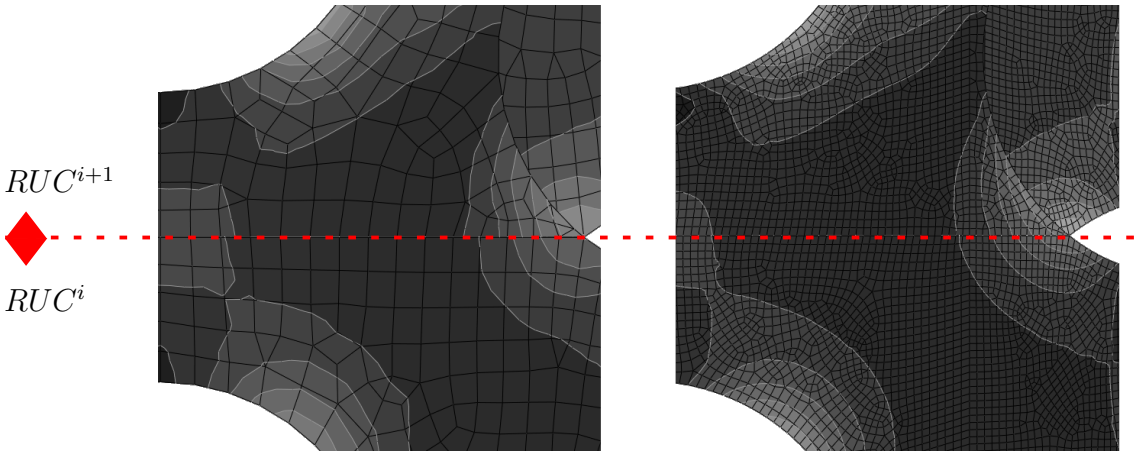

Figure 4.11.: Consideration of local shear stress field continuity at corresponding boundaries for a) a coarse mesh RUC arrangement and b) a fine mesh RUC arrangement. The view detail is defined corresponding to the dashed box in Fig. 4.9.

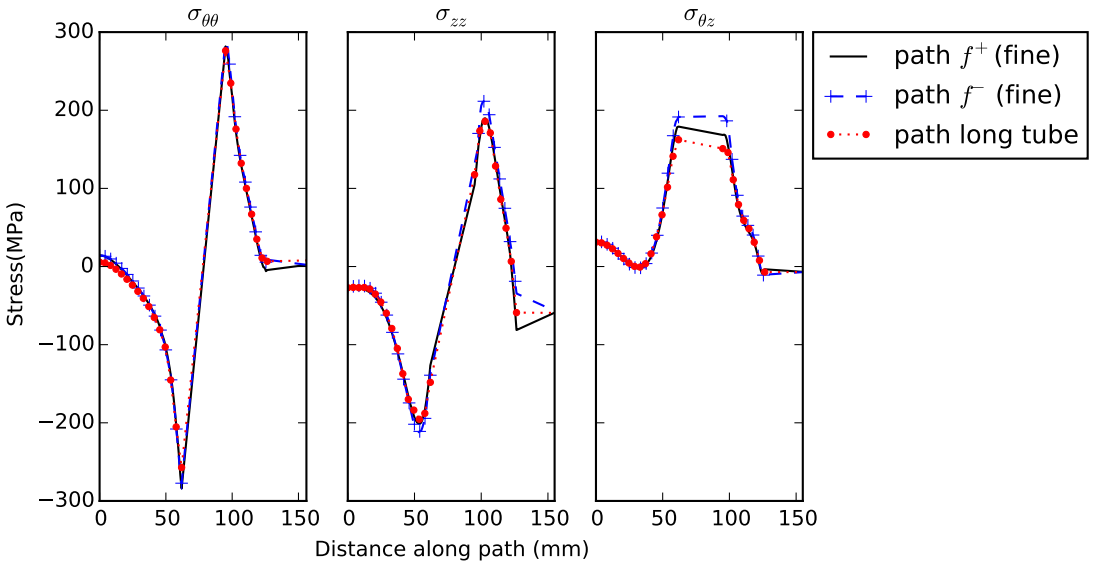

Figure 4.12.: Stress components $\sigma_{\theta\theta}$, σ_{zz}, $\sigma_{\theta z}$ along the first half of the paths defined in Fig. 4.8 for the RUC model with refined mesh.

A more detailed consideration of the stress field at the hole edges is obtained by comparing the three different types of hole intersections in the RUC to each other and to a hole of the long tube model. As the holes are arranged periodically along the circumference of the tube, an identical stress field is expected for all holes (see e.g. Fig. 4.9 b)). Since the unit cell intersects this periodic arrangement Fig. 4.8 shows three possible hole types A (eccentric intersection), B (no intersection) and C (centric intersection). Fig. 4.13 shows nearly congruent plot curves for the von Mises equivalent stress along the hole edges of the unit cell and the long tube model. The von Mises equivalent stress at the hole edges corresponds approximately to the circumferential stress component of the respective hole as the traction or the radial stress component, respectively, is approximately zero at these inner hole edges. The slightly lower peak stress in the case of the long tube model is attributed to the difference in mesh size.

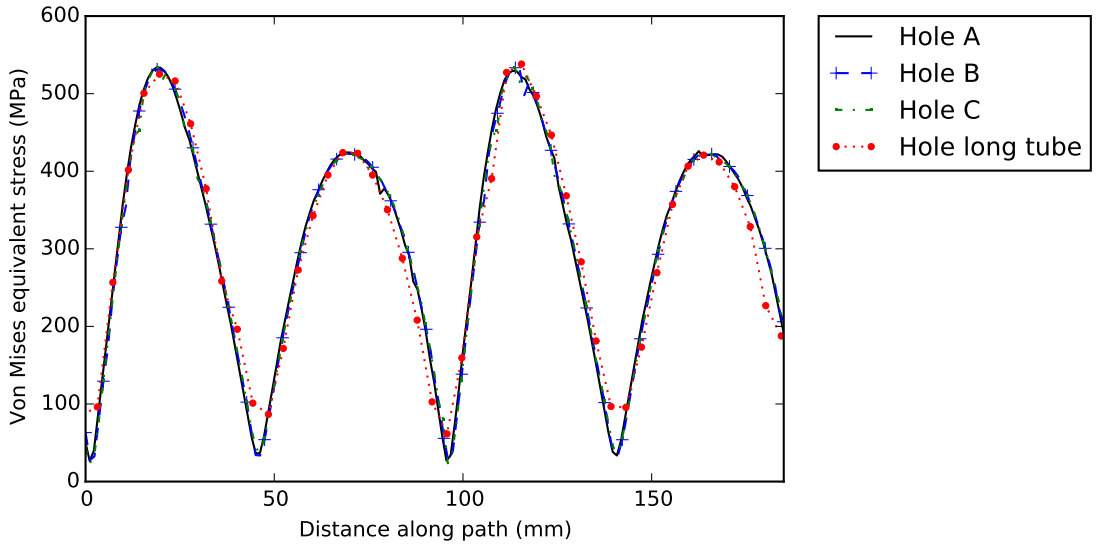

Figure 4.13.: Von Mises equivalent stress along the hole edges of different types of hole intersections in the RUC with refined mesh and one hole of the long tube model. See Fig. 4.8 for the definition of the hole paths.

This consideration of the local element size effects leads to the conclusion, that in the case of high requirements on the accuracy of the stress field representation the mesh quality on the boundaries of the RUC has to be taken into account, especially when the boundaries exhibit complex contours and high stress gradients are expected.

4.3.4. Plasticity

First, analogously to the previous sections, the structural response is examined by considering the load displacement curve, see left plot in Fig. 4.14. The dashed line represents the structural tensile tangent stiffness corresponding to the S_{11} entry in the stiffness matrix $\mathbf{S}$. In accordance with the values in Tab. 4.5 the tangent stiffness curve exhibits a constant part at a value of approximately $224 * 10^6 N$ for a load factor lower than $LF = 0.6$. A load factor of $LF = 1.0$ equals a maximum difference in displacement of the corresponding faces, f^+ and f^-, of $\Delta b_p^{max} = 0.2\text{mm}$. For a load factor higher than 0.6 the effect of the nonlinear material behaviour is perceptible and the tangent structural stiffness drops to a value of approximately $190 * 10^6 N$ for a load factor of $LF = 1.0$.

The right plot in Fig. 4.14 shows the curve of the recoverable strain energy per unit length and the plastic dissipation energy per unit length. These energy curves also manifest a representation of the effective properties and have to be preserved over the scales, meaning that long model and RUC have to exhibit the same energy values per unit length, cf. section 2.2. Corresponding to the load displacement curve the influence of plasticity becomes apparent in case for a displacement factor $LF > 0.6$ as the plastic dissipation energy exhibits nonzero values and the recoverable strain energy curve exhibits an inflection point. The good agreement of the curves resulting from the RUC model with the ones resulting from the long tube model suggest that the presented RUC approach is suited to

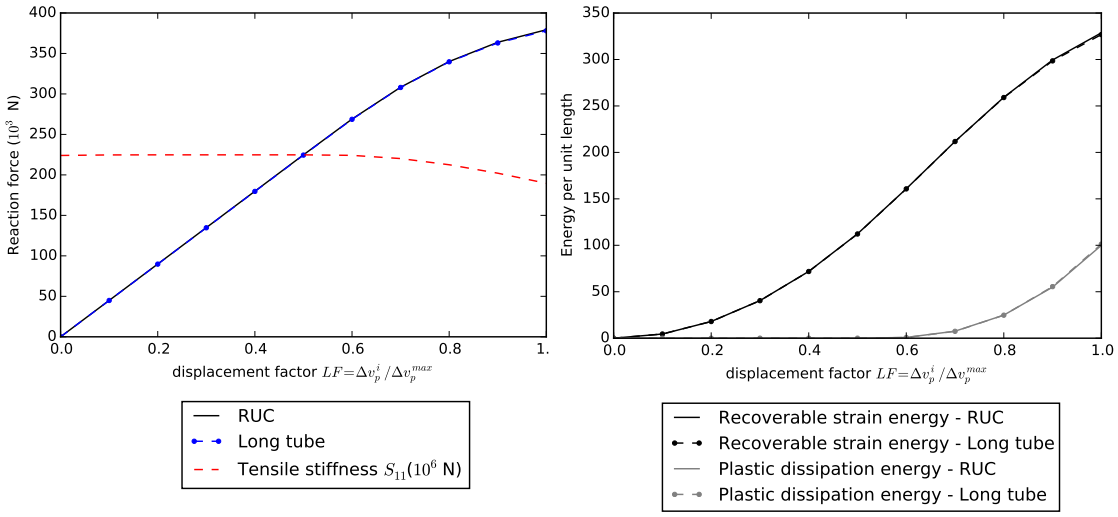

Figure 4.14.: Plots for the tensile displacement controlled loading with a elastic ideal plastic material behaviour for the RUC and the long tube model. Left: The reaction force at the control points and the resulting tensile tangent stiffness S_{11}. Right: Recoverable strain energy per unit length and plastic dissipation energy per unit length. The load factor represents a normalised measure defined as $LF = \Delta b_p^i / \Delta b_p^{max}$ with Δb_p^i being the displacement for the increment i.

examine the degradation of the effective structural properties due to non-localising nonlinearities such as plastic behaviour. However, care should be exercised as, in general, these effective properties cannot be applied to e.g. a beam element model in a homogenisation approach because an arbitrary load collective can no longer be seen as a linear combination of the four Euler-Bernoulli-St-Venant load cases. More precisely, non-localising nonlinearities can only be considered in a homogenisation approach when they result in stress and strain states that change in a consistent way for every point within a structure with an increase or decrease of the load factor.

In a second step, the stress field is examined. Fig. 4.15 shows a contour plot of the von Mises equivalent stress due to tensile loading comparing the unit cell with PBC (Fig. 4.15 a)) and a depicted segment of the long tube model (Fig. 4.15 b)). The von Mises equivalent stress field, which serves as reference for the yield stress in case of the present J2 plasticity, shows good agreement for the long tube model and the RUC model. Furthermore, Fig. 4.16 shows that the averaged stress field exhibits continuity at the corresponding boundaries, f^+ and f^-. Again, the slight deviations are interpreted as peculiarities of the displacement based FEM and its standard post-processing, cf. section 4.3.3.

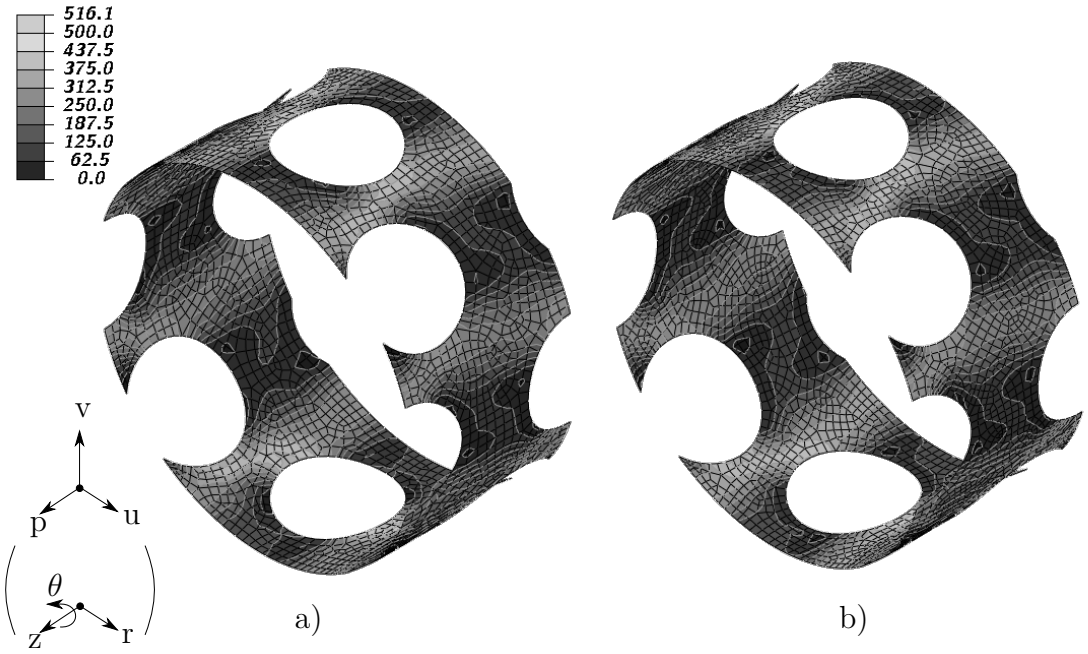

Figure 4.15.: Contour plot of von Mises equivalent stress due to tensile loading ($LF = 1.0$) with a linear-elastic ideal plastic material behaviour for a) the RUC model and b) a depicted segment of the long tube model. Values in the legend are in N/mm^2.

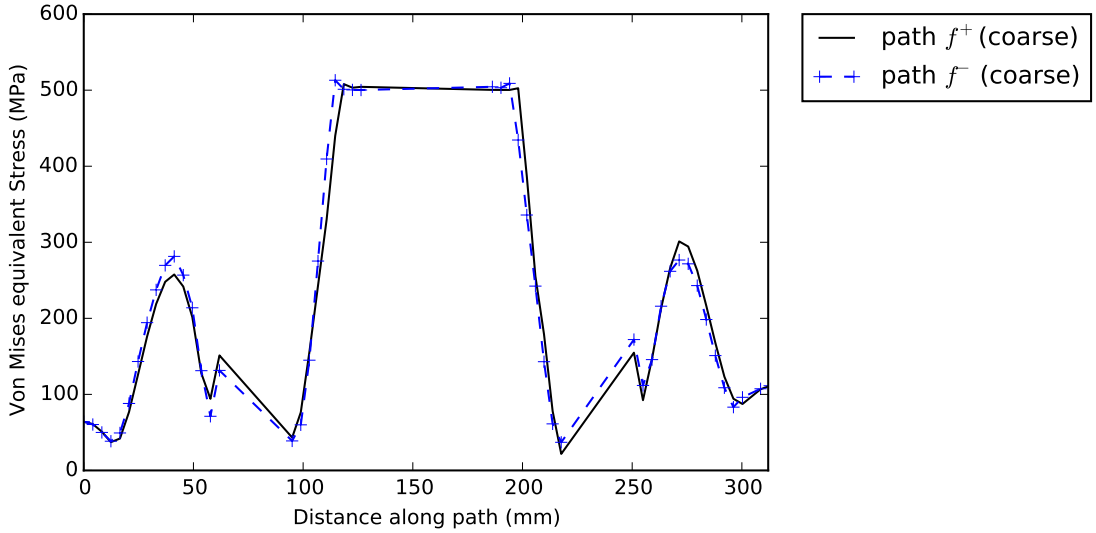

Figure 4.16.: Comparison of von Mises equivalent stress on corresponding boundaries due to tensile ($LF = 1.0$) loading of the coarse mesh unit cell and elastic ideal plastic material behaviour.

4.4. Further Applications

One possible application is to conduct fast parametric studies by combining an automated model generator with the automated PBC generator. This combination creates a series of alternative uniaxial RUCs in order to examine the effects of one or more parameters as e.g. the hole diameter in the case of the verification example of the perforated tube. Hence, better knowledge about the effects of different parameters or even an optimised structure is gained, without having to simulate the whole structure. Another useful application is the determination of the effective stiffness properties that are then applied to a large scale structure. Thus, a simple beam element model with the effective properties gained from a RUC can serve as a valid representation for complex frameworks that consist of multiple beam-like structures exhibiting a periodic arrangement of substructures along their axes.

In return, the results of this beam element model, i.e. the local difference in nodal displacements between two beam element nodes corresponding to the control points of the unit cell, can be reapplied to the unit cell in order examine small scale effects as e.g. local stress concentrations that may lead the onset of damage. A composite bike frame represents an example where the benefit of the described procedure comes to light. The consideration of a detailed composite tube segment as a RUC model yields accurate effective properties for the application to a beam element model of the bike frame. Thus, the structural response of the whole frame can be examined. In return, local effects as e.g. the onset of interlaminar damage can be investigated at different critical locations of the frame by reapplying the local deformation of the beam element model to the RUC. Another approach, for which no knowledge of the critical location is needed, uses the linear superposition of the basic unit cell responses as additional post-processing feature to determine the local margin of safety for the whole frame.

5. Summary

In light weight design, the simulation of uniaxial periodic structures represents an important class of product development methods that are needed to gain a detailed knowledge of complex structures under load. Making use of an internal periodic arrangement of substructures leads to an efficient modelling approach. A unit cell model of a single period is used to represent the large scale structure. The present work deals with the necessary theoretical concepts involved in such a link between the single period and the large scale structure for the uniaxial periodic case and how these concepts can be implemented for the practical use. More precisely, periodic boundary conditions (PBCs) are used to couple corresponding boundaries of the single period in order to gain a unit cell behaviour that accurately represents the large scale structure.

The first goal of this work is reached by deriving the theory for uniaxial periodic boundary conditions and to extend this theory for shell elements and nontrivial boundaries. Secondly, an automated generator of these periodic boundary conditions is programmed which enables the processing of a wide range of uniaxial repeating unit cells (RUCs). A graphical user interface is designed in order to facilitate the required input, which is needed to run the automated generator. The theory as well as the automated generator are tested by means of three example models of increasing complexity. The results are evaluated methodologically by examining the nodal displacements as well as the stiffnesses and stress fields. Multiple reference solutions from related research, analytical solutions or related FEM models are considered to verify the presented unit cell approach in combination

with the automated generator.

The nodal displacement components at the corresponding boundaries of the RUC subjected to PBC are compared for all verification examples. This comparison leads to the conclusion that geometric compatibility is given in the deformed state, meaning that no gaps or overlaps occur between fictitiously neighbouring unit cells.

The stiffness results represent the effective properties that are applied to a large scale structure in a homogenisation approach. The effective properties gained from the unit cell approach are consistent with those of the different reference solutions and in particular with the stiffness results of the large scale model. This leads to the conclusion that the presented periodic unit cell approach and its implementation present a valid homogenisation concept.

Additionally, the stress fields of the unit cell models exhibit good quality regarding the continuity at the corresponding boundaries as well as a good agreement in magnitude and distribution compared to the stress fields of the large scale reference model. This is not only an additional mean of verification of the correct representation by the unit cell but also shows how the presented method enables a localisation approach that allows a highly resolved consideration of small scale effects without having to simulate a highly detailed large scale model.

With respect to the computational expense, the run time of the FEM analysis of e.g. the long perforated tube model was approximately ten times higher for the linear elastic material and approximately 16 times higher for elastic ideal plastic material, when compared to the respective RUC model. This emphasises the importance of the presented method for models with a high number of unknowns and/or nonlinear behaviour.

All in all, a reliable tool is developed facilitating the simulation of complex beam like structures. A wide range of possible applications underlines the usefulness of

the presented approach and its numerical implementation.

5.1. Outlook

Despite the fact that the present work extended the theory and implementation for a wide a range of applications, the field still offers a number of unsolved problems or related theoretical concepts that can be applied to the case of uniaxial periodicity.

With respect to the torsional load case further research is needed to implement a periodic unit cell to represent correctly the case of warping torsion, where warping deformation is constrained.

In some cases the requirement of conformal meshes on the corresponding boundaries cannot be fulfilled or non conformal meshes are beneficial in some way. In order to circumvent this requirement, some concepts (see section 1.1.2) have been developed for the case of spatial periodicity. Applying these concepts to the class of uniaxial periodic problems would further extend the range of problems that can be handled with an automated generator.

Another extension with respect to the choice of unit cells that can be handled with the presented automated generator is finding a suitable algorithm for the processing of boundary contours with undercuts and edges parallel to the direction of periodicity.

Regarding the performance of the algorithm determining the nodes on the corresponding boundary faces, further optimisation or an alternative approach is required to establish a more efficient method for models with a high number of unknowns.

To sum up, a wide range of uniaxial periodic problems can be handled with the presented approach, although a number of possible problem types still require further research.

A. Manual - Uniaxial PBC Generator

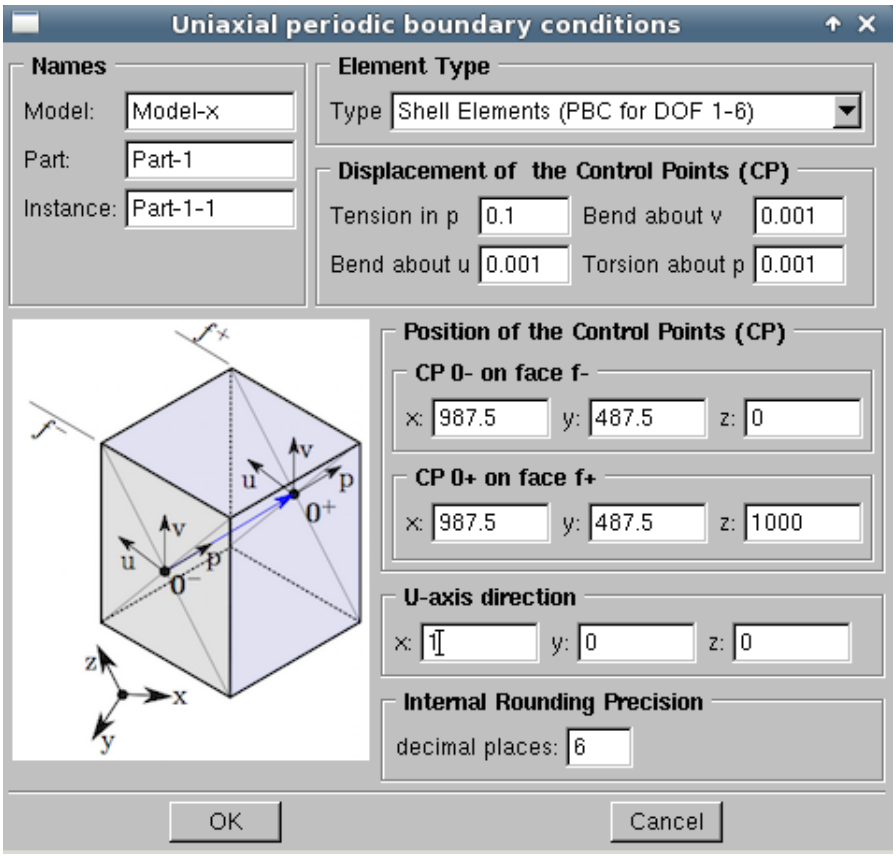

Figure A.1.: Input of data via RSG dialog for PBC generation

Prerequisites

The automated generator can be operated as a python script (`File -> Run Script`) or via the Graphical User Interface (`Plug-Ins -> UNIAXIAL PBC`). Both ap-

proaches require the same model prerequisites:

- The mesh needs to be defined in the part domain.
- The mesh needs to be conformal on the corresponding boundaries, i.e. the nodes on one face are in fact a projection of the nodes of the other face along the axis of periodicity.
- The respective material properties have to be defined and assigned to the mesh of shell elements or volume elements, respectively.
- The use of higher order elements, i.e. elements with a nonlinear trial function should work without any further adaptions. However, this has yet to be verified at an example.
- The model has to represent a valid uniaxial periodic unit cell. Geometric compatibility with fictitiously neighbouring unit cells has to be given for the undeformed state.
- The boundary contour must not exhibit edges or faces that are parallel to the direction of periodicity.
- Undercut contours can only be processed when occurring due to the intersection of a void resulting from the unit cell definition.
- An instance for the part has to be created.

Step by Step Guide

If the abovementioned requirements are fulfilled the following steps lead to the automated generation of the PBC and the ten load cases needed for the determination of the stiffness matrix $\mathbf{S}$ (at the example of graphical user interface plug in):

- Fill out the names for part, model and instance. (It is recommended to copy the respective name from the *Rename* context menu. When considering multiple models it is recommended to already name according to the default names.)

- Choose the element type modelling the corresponding boundaries. (It is possible to use a mixed element model. On the boundaries, however, it is necessary to use either shell or volume elements) For the shell element model only the standard shell element with 6 DOF per node is admissible for the generator.

- The displacement of the Control Points can be altered if desired. The value represents the absolute displacement of one control point leading to the difference in displacement of twice the value that is entered here. In other words, the displacement on the f^+ face corresponds to the negative displacement on f^-. The rotational displacement is given in radiants and should not exceed 0.05 for the small angle approximation to be valid which is the basis for the PBC.

- The Control Points are defined for both of the corresponding faces by giving the x,y,z coordinates. The vector connecting the control points defines the axis of periodicity. The distance of the control points has to coincide with the distance of the parallel faces of corresponding boundary faces.

- The u-axis is defined by giving its direction vector in x,y,z coordinates.

- The definition of the control points in combination with definition of the u-axis defines the reference coordinate system u,v,p of the unit cell which serves as the basis for the 4 basic load cases that eventually lead to effective properties according to these load cases. Hence, care should be exercised

when defining these parameters, as they are of particular importance for the correct behaviour of the unit cell.

- In a last step the decimal rounding precision can be altered from the default value of 6. This is only recommended when a first run of the generator showed that no boundary conditions have been generated or single node pairs have been omitted from the generation. This might be the case for models where the meshes on the boundaries are not conformal up to the defined rounding precision. Then the rounding precision needs to be lowered so that the algorithm is able to detect the conformal node pairs.

- Press Ok for the automated generator to start running. However, before the actual algorithm starts running an input check is performed. This input check examines whether values are missing or the input is inconclusive and provides an error message containing information on how to correct the error.

- The automated generator has now generated the periodic boundary conditions as well as all steps and the corresponding displacement controlled boundary conditions at the control points.

- For a correct representation of the displacement results all rigid body modes must be constrained by subjecting one or more mesh nodes to boundary conditions. Nodes that are part of the corresponding boundaries and thus coupled with an equation cannot be used for this rigid body movement constraint. Furthermore, these boundary conditions have to be chosen in way that no unphysical constraints occur, meaning that the results show no or negligible reaction forces at the respective nodes.

- According to a standard abaqus analysis, a job needs to be defined and submitted for analysis.

- If a determination of the effective properties is desired the script `poststiff.py` can to be run, see following section.

Postprocessing Script - Stiffness Matrix

The python script `poststiff.py` allows an automated post processing. This script basically reads out the strain energy at the end of every step and calculates the entries of the stiffness matrix according to section 2.2. The following model configurations and input is required :

- *model configuration*: The history output for the variable `Strain energy: ALLSE for Whole Model` has to be requested.
- *model configuration*: The load cases have to be defined in the following order corresponding to the matrix entries as it is done when utilising the PBC Generator:
  - `Initial`
  - `Step-S11` - tension in p
  - `Step-S12` - tension in p coupled with bending about u
  - `Step-S13` - tension in p coupled with bending about v
  - `Step-S14` - tension in p coupled with torsion about p
  - `Step-S22` - bending about u
  - `Step-S23` - bending about u coupled with bending about v
  - `Step-S24` - bending about u coupled with torsion about p
  - `Step-S33` - bending about v
  - `Step-S34` - bending about u coupled with torsion about p
  - `Step-S44` - torsion about p

- *input*: The path of the output database (.odb file) needs to be defined
- *input*: The length of the unit cell needs to be defined
- *input*: The displacements of b_p, ϕ_i of the unit cell sides need to be defined, when altered from the default values from the PBC Generator.

The stiffness matrix is calculated according to the unit system defined in the model (e.g. (N-mm) or (N-m)) and is written to the message area of Abaqus-CAE.

Bibliography

[1] http://classroom.materials.ac.uk/images/heli-fig3.jpg. 2015-06-01.

[2] http://www.carbonallotropes.com/carbon-nanotubes/39-single-wall-carbon-nanotubes.html. 2015-06-01.

[3] H. J. Boehm. A short introduction to basic aspects of continuum micromechanics. Technical report, ILSB TU Wien, 2014.

[4] N. Buannic and P. Cartraud. Higher-order effective modeling of periodic heterogeneous beams. i. asymptotic expansion method. *International Journal of Solids and Structures*, 38(40–41):7139 – 7161, 2001.

[5] P. Cartraud and T. Messager. Computational homogenization of periodic beam-like structures. *International Journal of Solids and Structures*, 43(3–4):686 – 696, 2006.

[6] C. E. Cesnik and D. H. Hodges. Vabs: A new concept for composite rotor blade cross-sectional modeling. *Journal of the American Helicopter Society*, 42(1):27–38, 1997.

[7] C. G. Dávila, P. P. Camanho, and A. Turon Travesa. Cohesive elements for shells. *© NASA TP Technical Reports, 2007, núm. 214869*, 2007.

[8] J. Dizy, R. Palacios, and S. T. Pinho. Homogenisation of slender periodic composite structures. *International Journal of Solids and Structures*, 50(9):1473 – 1481, 2013.

[9] J. Gager. *Modeling and simulation concepts for advanced braided composites*. PhD thesis, Vienna University of Technology (ILSB), 10 2013.

[10] J. Gager and H. Pettermann. Numerical homogenization of textile composites based on shell element discretization. *Composites Science and Technology*, 72(7):806 – 812, 2012.

[11] D. Gross, W. Hauger, J. Schröder, and W. Wall. *Technische Mechanik 2: Elastostatik*, pages 195–197. Springer-Lehrbuch. Springer Berlin Heidelberg, 2014.

[12] J. Hohe. A direct homogenisation approach for determination of the stiffness matrix for microheterogeneous plates with application to sandwich panels. *Composites Part B: Engineering*, 34(7):615 – 626, 2003.

[13] A. Kolpakov. Variational principles for stiffnesses of a non-homogeneous beam. *Journal of the Mechanics and Physics of Solids*, 46(6):1039–1053, 1998.

[14] C. Li and T.-W. Chou. A structural mechanics approach for the analysis of carbon nanotubes. *International Journal of Solids and Structures*, 40(10):2487 – 2499, 2003.

[15] T. Massart, B. Mercatoris, B. Piezel, P. Berke, L. Laiarinandrasana, and A. Thionnet. Multi-scale modelling of heterogeneous shell structures. *Computer Assisted Mechanics and Engineering Sciences*, 18:53–71, 2011.

[16] V.-D. Nguyen, E. Béchet, C. Geuzaine, and L. Noels. Imposing periodic boundary condition on arbitrary meshes by polynomial interpolation. *Computational Materials Science*, 55(0):390 – 406, 2012.

[17] D. Pahr. *Experimental and Numerical Investigations of Perforated FRP- Laminates*. PhD thesis, Vienna University of Technology (ILSB), 2003.

[18] D. H. Pahr and F. G. Rammerstorfer. Buckling of honeycomb sandwiches: periodic finite element considerations. *Computer modeling in engineering and sciences*, 3:229–241, 12 2006. ; 12,3.

[19] R. Palacios and C. E. S. Cesnik. Cross-sectional analysis of nonhomogeneous anisotropic active slender structures. *AIAA journal*, 43(12):2624–2638, 2005.

[20] J. Priebe. Stahlbau iii skriptum. Hamburg University of Technology (TUHH), 2010.

[21] Simulia Dassault Systèmes. *Abaqus Documentation*, 6.14 edition, 2014.

[22] D. Stegmair. *Ein Beitrag zur Wölbkrafttorsion inhomogener Balken*. PhD thesis, Fakultät für Leichtbaustrukturen Universität der Bundeswehr München, 2014.

[23] Wiedmann. *Leichtbau Elemente und Konstruktion*, volume 1, chapter 3. Springer, 2007.

[24] J. Wippler, S. Fünfschilling, F. Fritzen, T. Böhlke, and M. J. Hoffmann. Homogenization of the thermoelastic properties of silicon nitride. *Acta Materialia*, 59(15):6029 – 6038, 2011.

[25] W. Wu, J. Owino, A. Al-Ostaz, and L. Cai. Applying periodic boundary conditions in finite element analysis. In *Simulia Community Conference*, pages 707–719. University of Tennessee Chattanooga, University of Mississippi, 2014.